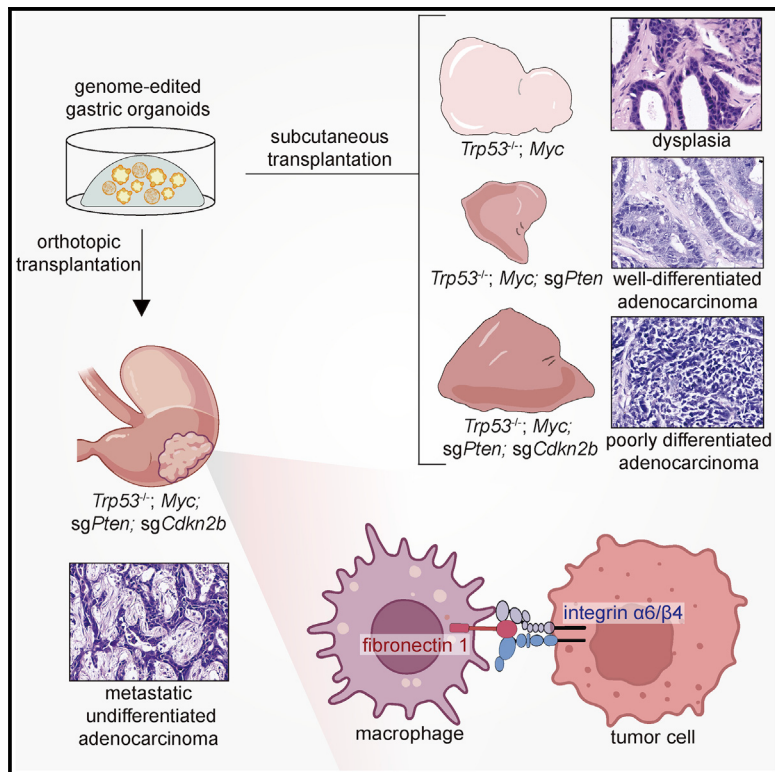


Dissecting the genetic and microenvironmental factors of gastric tumorigenesis in mice

Graphical abstract



Authors

Zhenghao Lu, Ailing Zhong,
Hongyu Liu, ..., Jiankun Hu, Yu Liu,
Chong Chen

Correspondence

hujkwch@126.com (J.H.),
yuliuscu@scu.edu.cn (Y.L.),
chongchen@scu.edu.cn (C.C.)

In brief

Lu et al. establish a series of genetics-defined gastric cancer models to investigate the stepwise tumorigenesis from dysplasia to well-differentiated, poorly differentiated, and metastatic gastric adenocarcinoma in mice. It is shown that the interaction between macrophages and tumor cells through fibronectin and integrin $\alpha 6\beta 4$ promotes gastric cancer progression and metastasis.

Highlights

- Gene-edited gastric organoids generate primary gastric cancers (GC) in mice
- Different genetic drivers result in different stages of GC
- Orthotopic-specific macrophages promote GC progression
- Macrophages interact with tumor cells through the fibronectin-integrin interaction



Article

Dissecting the genetic and microenvironmental factors of gastric tumorigenesis in mice

Zhenghao Lu,^{1,4} Ailing Zhong,^{2,4} Hongyu Liu,^{2,4} Mengsha Zhang,^{2,4} Xuelan Chen,² Xiangyu Pan,² Manli Wang,² Xintong Deng,² Limin Gao,³ Linyong Zhao,¹ Jian Wang,² Yi Yang,² Qi Zhang,² Baohong Wu,² Jianan Zheng,² Yigao Wang,¹ Xiaohai Song,¹ Kai Liu,¹ Weihan Zhang,¹ Xiaolong Chen,¹ Kun Yang,¹ Xinzu Chen,¹ YingLan Zhao,² Chengjian Zhao,² Yuan Wang,² Lu Chen,² Zongguang Zhou,¹ Jiankun Hu,^{1,*} Yu Liu,^{2,*} and Chong Chen^{1,5,*}

¹Gastric Cancer Center and Laboratory of Gastric Cancer, State Key Laboratory of Biotherapy, West China Hospital, Sichuan University, Chengdu, Sichuan 610041, China

²State Key Laboratory of Biotherapy, West China Hospital, Sichuan University, Chengdu, Sichuan 610041, China

³Department of Pathology, West China Hospital, Sichuan University, Chengdu, Sichuan 610041, China

⁴These authors contributed equally

⁵Lead contact

*Correspondence: hujkwch@126.com (J.H.), yuliuscu@scu.edu.cn (Y.L.), chongchen@scu.edu.cn (C.C.)

<https://doi.org/10.1016/j.celrep.2022.111482>

SUMMARY

Gastric cancer (GC) is one of the most frequent and lethal malignancies in the world. However, our understanding of the mechanisms underlying its initiation and progression is limited. Here, we generate a series of primary GC models in mice with genome-edited gastric organoids, which elucidate the genetic drivers for sequential transformation from dysplasia to well-differentiated and poorly differentiated GC. Further, we find that the orthotopic GC, but not the subcutaneous GC even with the same genetic drivers, display remote metastasis, suggesting critical roles of the microenvironment in GC metastasis. Through single-cell RNA-seq analyses and functional studies, we show that the interaction between fibronectin 1 on stomach-specific macrophages and integrin α6β4 on GC cells promotes remote metastases. Taken together, our studies propose a strategy to model GC and dissect the genetic and microenvironmental factors driving the full-range gastric tumorigenesis.

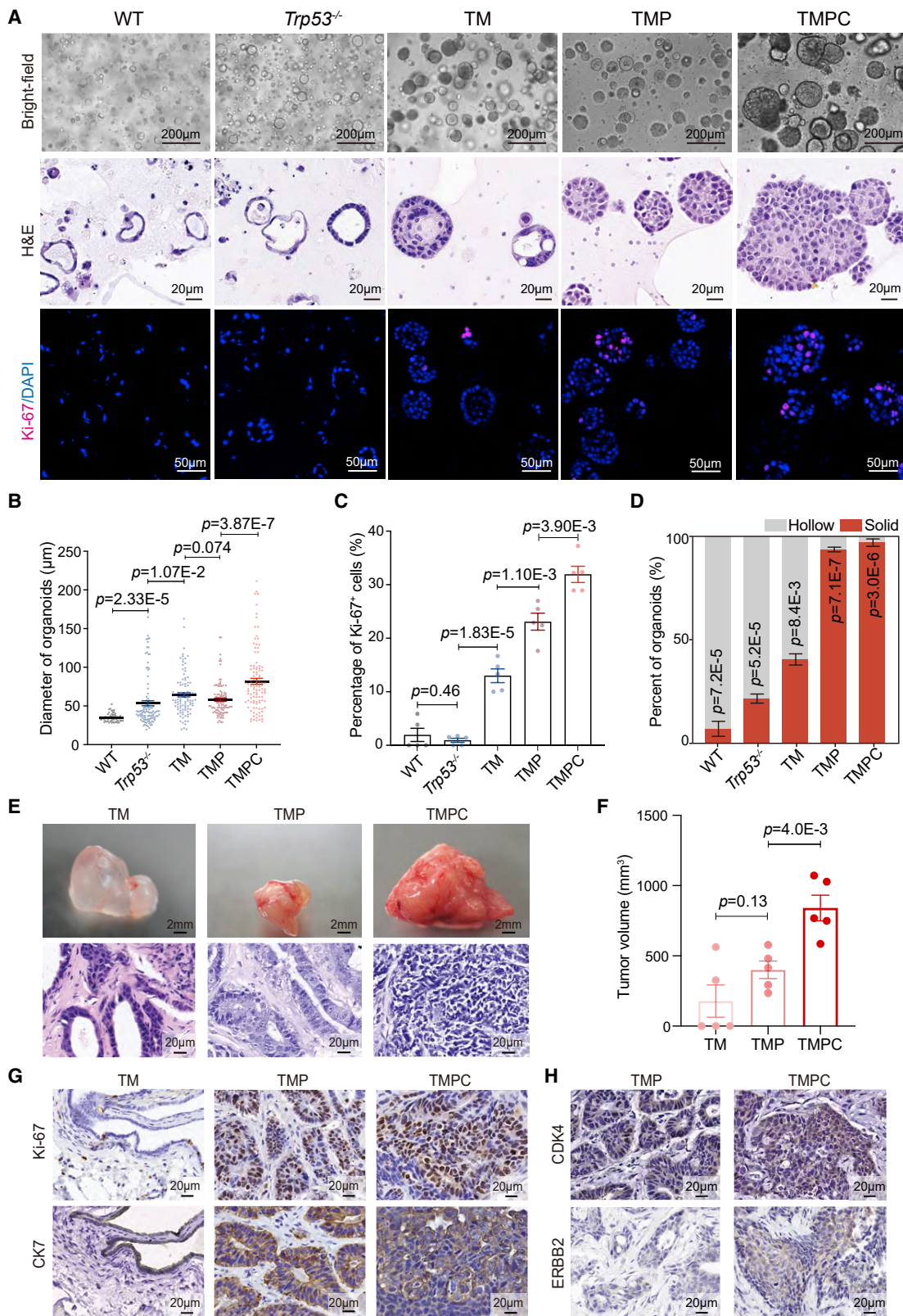
INTRODUCTION

Carcinogenesis is proposed to be a multistage process for cells to progress from normalcy to malignancy, which might explain up to several decades' latencies in patients (Cooper, 2000). Accumulating evidence suggests that various factors, including pre-tumor and tumor cell-intrinsic genetic abnormalities and microenvironmental dysregulations, contribute to each step of this gradual transformation process. One example is demonstrated in a genetic model of colon cancer. It shows that the sequential mutations in APC, KRAS, TP53, and SMAD4 drive colon epithelial cells transforming into dysplasia, adenoma, carcinoma, and eventually metastatic cancer (Fearon and Vogelstein, 1990; Vogelstein et al., 2013). The next-generation sequencing analyses reveal more and more genetic mutations, which can be either driver mutations or passenger mutations, in human cancers of different stages. However, whether and how these mutations promote the initiation and progression of cancers remains to be elucidated. Further, not only these factors intrinsic of tumor cells, but also the tumor microenvironment plays a critical role in tumorigenesis and progression (Anderson and Simon, 2020; Chen and Song, 2022). There is emerging evidence indicating that both systemic and microenvironmental factors play critical roles in all steps of tumorigenesis. For example, can-

cer-associated macrophages can promote progression and metastasis through various mechanisms in different cancers, including secreting cytokines, growth factors, and oxygen (Pollard, 2004; Qian and Pollard, 2010). And tissue damages can promote the initiation and progression of pancreatic ductal adenocarcinoma through a gene-environment-induced epigenetic reprogramming (Alonso-Curbelo et al., 2021). Neutrophil extracellular traps promote the metastasis of breast and colon cancers through the interaction of NET-DNA and CCDC25 of tumor cells (Yang et al., 2020). A large amount of effort is required to further dissect these intrinsic and extrinsic factors during the whole process of carcinogenesis, especially in some types of cancers so far less studied.

Gastric cancer (GC) is one of such obviously disproportionately less studied human cancers. It is the fifth most common cancer in the world and kills about 1 million people per year (Sung et al., 2021). It is more common in East Asia, including China. The risk factors for GC include *Helicobacter pylori* infection, diet, smoking, and inherited and non-inherited genetics (He et al., 2021). Recently genomic analyses of large cohorts of GC patients show that deficiency of tumor suppressors, such as TP53, CDKN2B, CDH1, ARID1A, and PTEN, through mutations, deletions, and/or DNA methylation, and gain-of-function mutations or amplification of oncogenes, such as ERBB2,





(legend on next page)

MYC, and *KRAS*, are among the most frequent genetic abnormalities associated with GC in patients (Cancer Genome Atlas Research, 2014; Cristescu et al., 2015; Nagaraja et al., 2019; Wang et al., 2014; Yeoh and Tan, 2022). These mutations might have an impact on the initiation, progression, metastasis, and clinical outcomes of the disease. The combination of oncogenic *KRAS*^{G12D} and loss of *CDH1* and *TP53* gives rise to aggressive gastric adenocarcinoma with metastases in multiple organs (Till et al., 2017). And intriguingly, disruption of *TP53* and *ARID1A* in human organoids leads to GC with a diffused type once transplanted into mice (Lo et al., 2021). Studies on patient-derived tumor organoids show that knockout of *TP53* and *CDH1* in wild-type gastric organoids was sufficient to allow culture without R-spondin even though these organoids were still dependent on exogenous Wnt-3A (Nanki et al., 2018). However, despite these signs of progress, our understanding of the molecular mechanisms underlying GC initiation and progression is still very limited, which hampers the development of new treatments for this lethal malignancy.

Animal models of GC, which can represent the whole transforming process of carcinogenesis from normal epithelial cells to metastatic cancer cells, are critical to dissect the underlying pathology and molecular mechanisms. Although genetically engineered mouse models have significantly contributed to the basic and translational studies on GC, they are time-consuming, costly, and technically inconvenient (Seidlitz et al., 2019; Yu et al., 2014). Recent progress in organoid culture and genome editing provides an alternative strategy to generate cancer models more efficiently (Na et al., 2022; O'Rourke et al., 2017; Pan et al., 2022; Roper et al., 2017; Wang et al., 2022). Here, we applied a similar strategy to model GC in mice. And with these models, we dissected the genetic and microenvironmental drivers for GC from dysplasia to well-differentiated carcinoma, poorly differentiated carcinoma, and metastatic cancer.

RESULTS

The function of GC-related genetic drivers in premalignant gastric organoids

Given the recent progress in cancer modeling with gene-edited organoids, we decided to generate GC with this technique in mice (Figure S1A). Briefly, normal gastric epithelial organoids were derived from the stomach of Cas9-EGFP mice (Platt et al., 2014). sgRNAs and cDNA were introduced into these organoids to disrupt the potential GC-related tumor suppressor

genes and overexpress oncogenes, respectively. Then these gene-edited gastric organoids were transplanted into the recipient mice, of which tumorigenesis was monitored. We analyzed the genetic landscape, including mutations (truncating, in frame, missense, and splice site mutation), copy number variations (shallow deletion, deep deletion, gain, and amplification), and structural variations, of 1,590 GC samples from the cBioPortal dataset (<https://www.cbiportal.org/>). *TP53* was one of the most frequently altered genes (Cancer Genome Atlas Research, 2014), which was disrupted in up to 56% of GC patients. *PTEN* and *CDKN2B* were also among the most frequently altered genes in human GC, with mutation ratios of 25% and 34%, respectively. *MYC* was amplified in 55% of patients (Figure S1B; Table S1). Remarkably, these alterations tended to co-occur in GC patients (Figure S1C; Table S1). About 9% of all GC patients harbored *TP53*, *MYC*, *PTEN*, and *CDKN2B* variations together (Figure S1D; Table S1). Therefore, we decided to test the roles of these genes and their combinations in gastric tumorigenesis.

We cultured gastric organoids from young adult *Trp53*^{-/-}; Cas9-EGFP mice in 3D Matrigel. sgRNAs against *Pten* and *Cdkn2b*, linked with mCherry, and *Myc* cDNA, linked with luciferase, were introduced into these organoids (Figure S1E). Luciferase and mCherry could facilitate detecting the tumors derived from these organoids. Compared with those from wild-type (WT) animals, *Trp53*^{-/-} organoids had significantly increased size (Figures 1A and 1B). Then, we introduced *Myc* cDNA and the luciferase reporter gene into *Trp53*^{-/-} organoids (Figure S1F). The proliferation of *Trp53*^{-/-}; *Myc* (TM) organoids was significantly accelerated compared with *Trp53*^{-/-} organoids, indicated by Ki-67 staining (Figures 1A and 1C). Further, we mutated *Pten* in the TM organoids (TMP) (Figures S1G and S1H). And there was a significant increase of Ki-67⁺ cells in the TMP organoids compared with the TM organoids (Figure 1C). Further, *Cdkn2b* was disrupted by sgRNA, which further increased the size and percentage of Ki-67⁺ cells in the *Trp53*^{-/-}; *Myc*; sg*Pten*; sg*Cdkn2b* (TMPC) organoids (Figures 1A–1C and S1G). Interestingly, most of the WT gastric organoids were hollow, similar to previous reports (Barker et al., 2010; Stange et al., 2013), while there were significantly increased solid organoids in the *Trp53*^{-/-}, TM, TMP, and TMPC groups (Figures 1A and 1D). Previous reports suggested that solid organoids might contain more stem cell-like cells in some types of organoids (Broutier et al., 2017; Santos et al., 2019). Immunofluorescence staining showed that most of the cells in solid gastric organoids were SOX2 and LGR5 positive while, in contrast, only a few of them in the hollow

Figure 1. Modeling gastric cancers of different stages with CRISPR-Cas9-mediated engineered gastric organoids in mice

- (A) Representative bright-field (top) images and H&E (middle), and immunofluorescence staining of Ki-67 (bottom) in WT, *Trp53*^{-/-}, TM (*Trp53*^{-/-}; *Myc*), TMP (*Trp53*^{-/-}; *Myc*; sg*Pten*), TMPC (*Trp53*^{-/-}; *Myc*; sg*Pten*; sg*Cdkn2b*) mouse gastric organoids. Scale bar, 200 μm (top), 20 μm (middle), and 50 μm (bottom).
- (B) The diameters of WT, *Trp53*^{-/-}, TM, TMP, and TMPC gastric organoids. Data presented as the means ± the SEM; p value was calculated by unpaired t test.
- (C) The percentages of Ki-67⁺ cells in WT (n = 5), *Trp53*^{-/-} (n = 5), TM (n = 5), TMP (n = 5), and TMPC (n = 5) gastric organoids. Data presented as the means ± the SEM; p value was calculated by unpaired t test.
- (D) The percentages of hollow and solid organoids in WT, *Trp53*^{-/-}, TM, TMP, and TMPC organoids. Data presented as the means ± the SEM; p value was calculated by unpaired t test.
- (E) Representative bright-field (top) and H&E (bottom) images in the TM, TMP, and TMPC subcutaneous tissues. Scale bar, 2 mm (top) and 20 μm (bottom).
- (F) Statistical graph showing the volume of the subcutaneous TM, TMP, and TMPC tissues (n = 5). Data presented as the means ± the SEM; p value was calculated by unpaired t test.
- (G) Representative Ki-67 (top) and CK7 (bottom) staining of the subcutaneous TM, TMP, and TMPC tissues. Scale bar, 20 μm.
- (H) Representative CDK4 (top) and ERBB2 (bottom) staining of the subcutaneous TMP and TMPC tissues. Scale bar, 20 μm.

organoids (Figures S1I–S1K). These results suggested that the TMP and TMPC organoids might have increased stemness.

Modeling the stepwise tumorigenesis of GC in mice

To test the tumorigenesis capacity of these premalignant organoids *in vivo*, we transplanted them into nude mice subcutaneously (Figure S1A). Two months after transplantation, two out of five recipient mice with TM organoids formed bulges at the injection sites. They displayed porous structures with dysplastic polypoid epithelium. Instead, all five mice with TMP organoids developed tumors. Histological analyses indicated the TMP tumors as well-differentiated adenocarcinoma. All the recipients of the TMPC organoids developed aggressive tumors, which, in contrast, displayed features of poorly differentiated adenocarcinoma (Figure 1E). And the TMPC tumors grew significantly faster than the TMP tumors (Figures 1E, 1F, S1L, and S1M). Immunohistochemistry (IHC) staining confirmed the expressions of CK7, Ki-67, CDK4, and ERBB2, diagnostic markers of human GC, in TMP and TMPC tumors (Figures 1G and 1H) (Birkman et al., 2018; Ko et al., 2017). These results demonstrated that gastric organoids with GC-associated mutations were able to initiate malignancies in mice, and genetic drivers significantly affected the malignancy of the resulting tumors.

Generating primary and orthotopic TMPC GC in mice

Then we set to generate primary and orthotopic GC. The premalignant TMPC organoids were introduced into the submucosa of the recipient's stomach (Figure S2A). Luciferase living image detected specific signal of the transplanted organoids as early as 1 week after transplantation, and the luciferase intensity increased over time, indicating the rapid growth of the transplant (Figure 2A). About 1–2 months later, these recipient mice displayed severe body weight loss and cachexia, typical syndromes associated with GC patients (Figures S2B and S2C). Biopsy dissection showed that solid tumors were formed at the injection site on the stomach. Those tumors were mCherry positive, indicating that they were derived from the transplanted TMPC organoids (Figure 2B). Histologic analyses revealed that these tumors were poorly differentiated adenocarcinoma, positive for Ki-67, CK7, and EPCAM staining (Figure 2C).

Importantly, despite the histologic similarity of the subcutaneous and orthotopic tumors derived from the same TMPC organoids, we found that there were massive distal metastases in the recipients with orthotopic tumors, with no detectable metastases in those with subcutaneous tumors (Figures 2D, 2E, S2D, and S2E). Histologic analyses confirmed that these metastases originated from the orthotopic TMPC tumors (Figure S2F). Tumor organoids were cultured from the subcutaneous and orthotopic TMPC tumors. Interestingly, orthotopic tumor organoids, but not subcutaneous ones, displayed multiple protrusion structures, which had been suggested to be associated with metastasis capacity in small cell lung cancer (Na et al., 2022; Yang et al., 2019) (Figure 2F). These results strongly indicated that orthotopic GCs had significantly increased metastasis capacity compared with subcutaneous tumors, even though they were derived from the same premalignant gastric organoids with the same genetic drivers.

Transcriptome analyses of the GC models of different stages

To characterize molecular features of these GCs, we performed transcriptome analyses of those tissues derived from TM, TMP, and TMPC subcutaneous tumors. RNA-seq data confirmed that *Pten* and *Cdkn2b* had been disrupted in tumor tissues (Figure S3A). And the heatmap of differentially expressed genes suggested that TM tissues were distinct from TMP and TMPC tissues (Figure 3A; Table S2). Gene ontology (GO) pathways significantly enriched in TM groups were related to tissue homeostasis, gland morphogenesis, and morphogenesis of a branching epithelium, consistent with their largely normal morphology (Figures 3A and 3B). And multiple extracellular matrix related pathways were enriched in TMP groups, while DNA replication, positive regulation of cell cycle process, and EMT pathway were enriched in TMPC groups, supporting them as a more aggressive malignancy (Figure 3B). Consistent with their histology, TMPC tumors showed the highest poorly differentiated scores (Rhodes et al., 2004). And in line with their fast growth, they also expressed high levels of cell cycle genes (Figure 3C; Table S3). Importantly, the TM gene signature mimicked that of tumor-adjacent normal tissues, while, in contrast, those of TMP and TMPC tumors were similar to that of GC in the stomach adenocarcinoma cohort of The Cancer Genome Atlas Program (TCGA-STAD) (Figure S3B). And further, GC patients with high expressions of the TMPC gene signature had significantly poorer prognoses than those with high expressions of the TMP gene signature (Figure S3C).

Importantly, the orthotopic TMPC tumors were clearly separated from the subcutaneous TMPC ones by PCA (Figure 3D). The upregulated and downregulated genes in the orthotopic TMPC tumors, compared with the normal gastric epithelium, were significantly positively and negatively, respectively, enriched in human GC (NES = 1.46, $q = 0.00$, and NES = −1.72, $q = 0.00$, respectively) (Figure S3D) (Li et al., 2018). Canonical carcinoma marker genes were highly expressed in orthotopic TMPC tumors, such as *Mki67*, *Brcal*, *Egfr*, *Ceacam1*, *Ceacam2*, etc., while markers for the normal gastric epithelium, such as *Cdh1*, *Tff1*, *Tff2*, *Gkn1*, and *Gkn2*, were significantly downregulated in orthotopic TMPC tumors (Figure S3E). There were 3,125 and 1,258 genes up- and downregulated, respectively, in orthotopic TMPC tumors compared with subcutaneous ones (Figure 3E; Table S2). Among the upregulated ones were those related to epithelium-mesenchymal transition and cell migration-related genes, such as *Fgf2*, *Wnt5a*, *Mmp2*, *Ccr2*, *Ccr3*, *Cxcl10*, and *Itgb4* (Figure 3E; Table S2). Gene set enrichment analysis (GSEA) showed that multiple metastasis-related pathways were significantly positively enriched in the orthotopic TMPC tumors comparing to the subcutaneous ones (Figure 3F).

Single-cell transcriptome profiling of the subcutaneous and orthotopic TMPC tumors

To gain a deep insight into the cellular and molecular differences between TMPC tumors developed subcutaneously and orthotopically, we performed single-cell RNA sequencing analyses with 10x Genomics (Figure 4A and S4A; Table S4). Classic marker genes were used to identify each population, such as *S100a8* and *S100a9* for neutrophils, *Lyz2* and *Csf1r* for

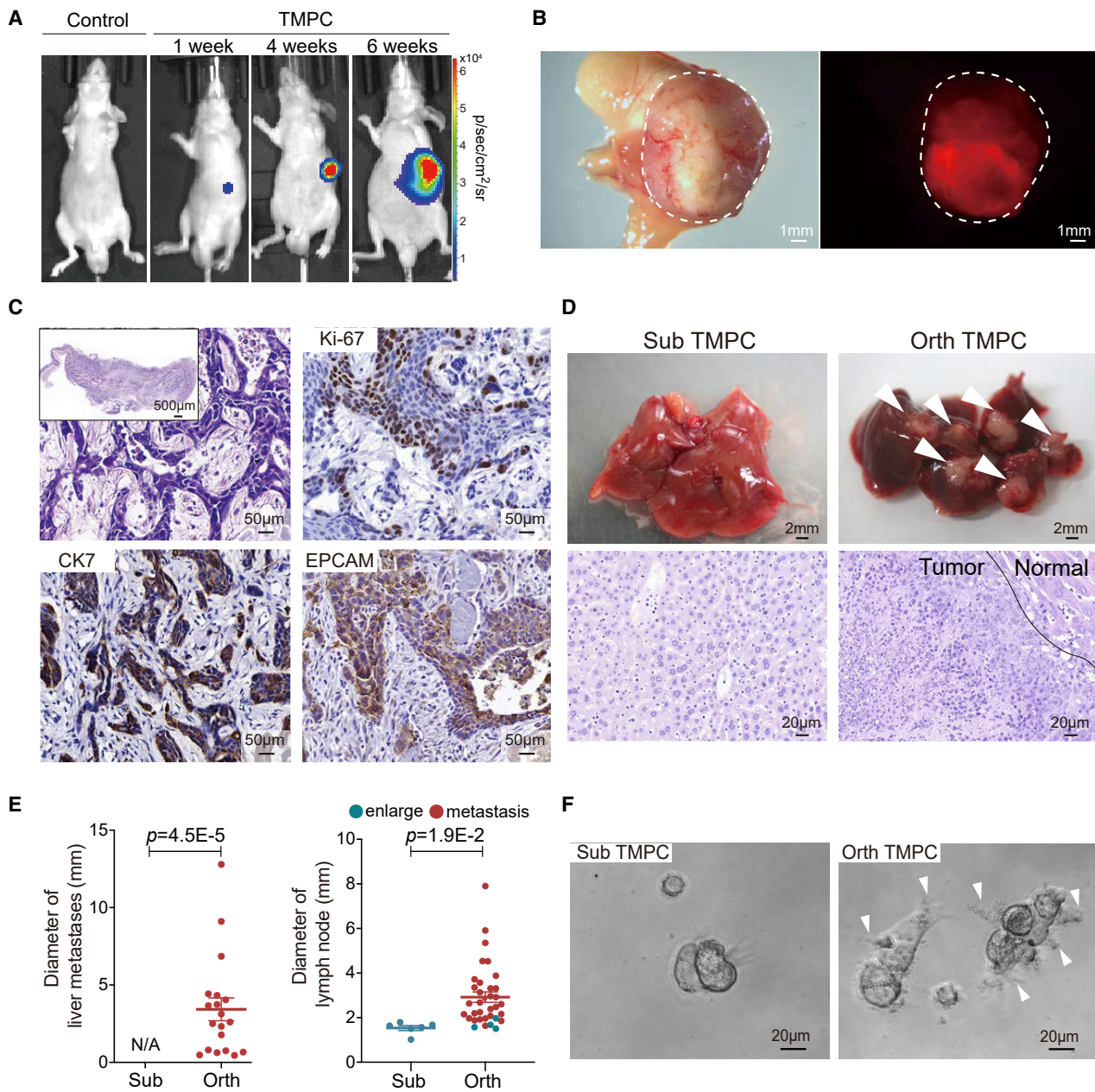


Figure 2. Orthotopic TMPC tumors display distal metastases

- (A) Representative bioluminescent images of the orthotopic TMPC mice at 1, 4, and 6 weeks.
- (B) Representative bright-field (left) and red fluorescent (right) images of the orthotopic TMPC tumor. Scale bar, 1 mm. Circled areas indicate the tumor regions.
- (C) Representative H&E, Ki-67, CK7, and EPCAM staining of the orthotopic TMPC tumors. Scale bar, 50 μ m. Box area showing lower magnification. Scale bar, 500 μ m.
- (D) Representative bright-field (top) images and H&E staining (bottom) of liver from subcutaneous (left) and orthotopic (right) TMPC mice. Scale bar, 2 mm (top) and 20 μ m (bottom).
- (E) The diameters of subcutaneous and orthotopic TMPC mice ($n = 9$) showing visible liver (left) and lymph node (right) metastases. Each dot indicates a metastasis (red) or enlarge (blue) locus. Data presented as the means \pm the SEM; p value was calculated by unpaired t test.
- (F) Representative images showing the morphologies of the subcutaneous (left) and orthotopic (right) TMPC tumor cells in 2D culture. Arrowheads indicate the protrusion structures. Scale bar, 20 μ m.

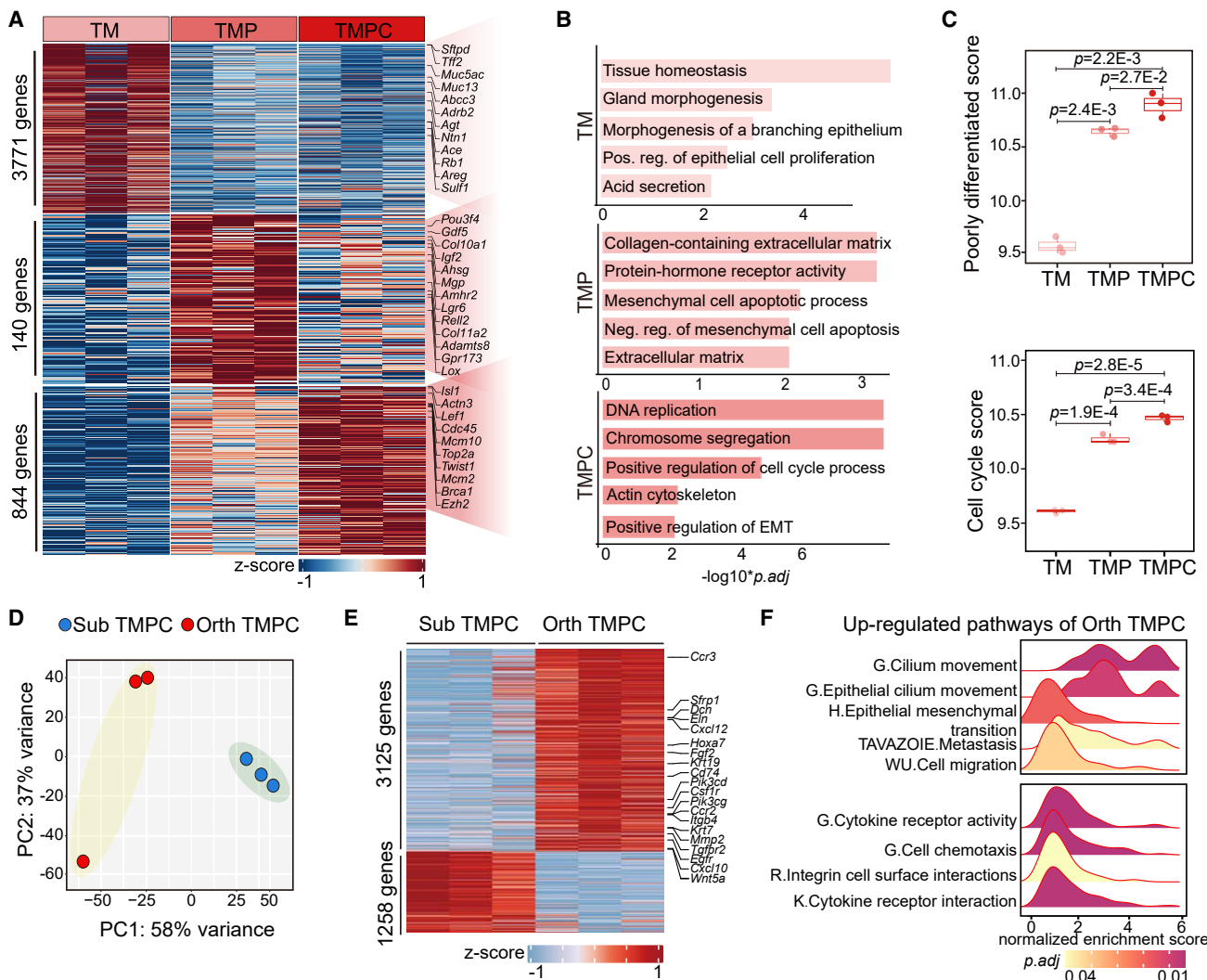


Figure 3. Transcriptome analyses of GC models of different stages

- (A) The heatmap showing TM, TMP, and TMPC significant high expression gene patterns. Homeostasis maintenance, extracellular matrix, proliferation, and invasion-associated genes are labeled on the right.
- (B) Gene ontology enrichment analyses of the TM, TMP, and TMPC signature genes.
- (C) The boxplots showing the poorly differentiated (top) and cell cycle (bottom) scores in TM ($n = 3$), TMP ($n = 3$), and TMPC ($n = 3$) tumors. Two-tailed unpaired t test was performed to determine the significant level.
- (D) The dot plot showing principal component analysis result of RNA-seq data from subcutaneous and orthotopic TMPC tumors.
- (E) The heatmap presenting 3,125 upregulated and 1,258 downregulated genes in orthotopic TMPC tumors comparing with subcutaneous ones ($p < 0.05$ and absolute \log_2 fold-change > 1). Crucial genes were labeled on the right.
- (F) The ridge plot showing positive enriched pathways in orthotopic TMPC tumors by GSEA (G: GO, H: Hallmark, R: Reactome, K: KEGG).

macrophages, *Col1a1* for fibroblasts, and *Pecam1* and *Egf17* for endothelium (Figures 4B and S4B). Normal gastric mucosa epithelial cells, identified with *Gkn2*, *Tff1*, and *Tff2* expressions, were only detected in the orthotopic tumor sample (Figure S4B). Strikingly, the singleR annotated analyses revealed that all of these populations in the mouse tumors were highly and specifically correlated with those in GC patients (Sathe et al., 2020) (Figures 4C and S4C; Table S3). The relative proportions of non-tumor cells in the orthotopic tumor were larger than those of the subcutaneous tumor (Figure 4D; Table S4). And consis-

tently, orthotopic tumors possessed much higher putative protein-protein interaction potency (Figure 4E; Table S4). The orthotopic tumor cells, enriched in cluster 0, expressed high levels of genes associated with metastasis stage (M1) in human GC (Figure 4F; Table S3). Importantly, the gene signature of the orthotopic tumor cells, compared with the subcutaneous ones, and that of the cluster 0 were enriched in human GC with metastases (Figure 4G). Consistent with their enhanced metastatic capacity, the pathways positively enriched in the orthotopic tumor cells included the EMT pathway, the podosome regulation pathway,

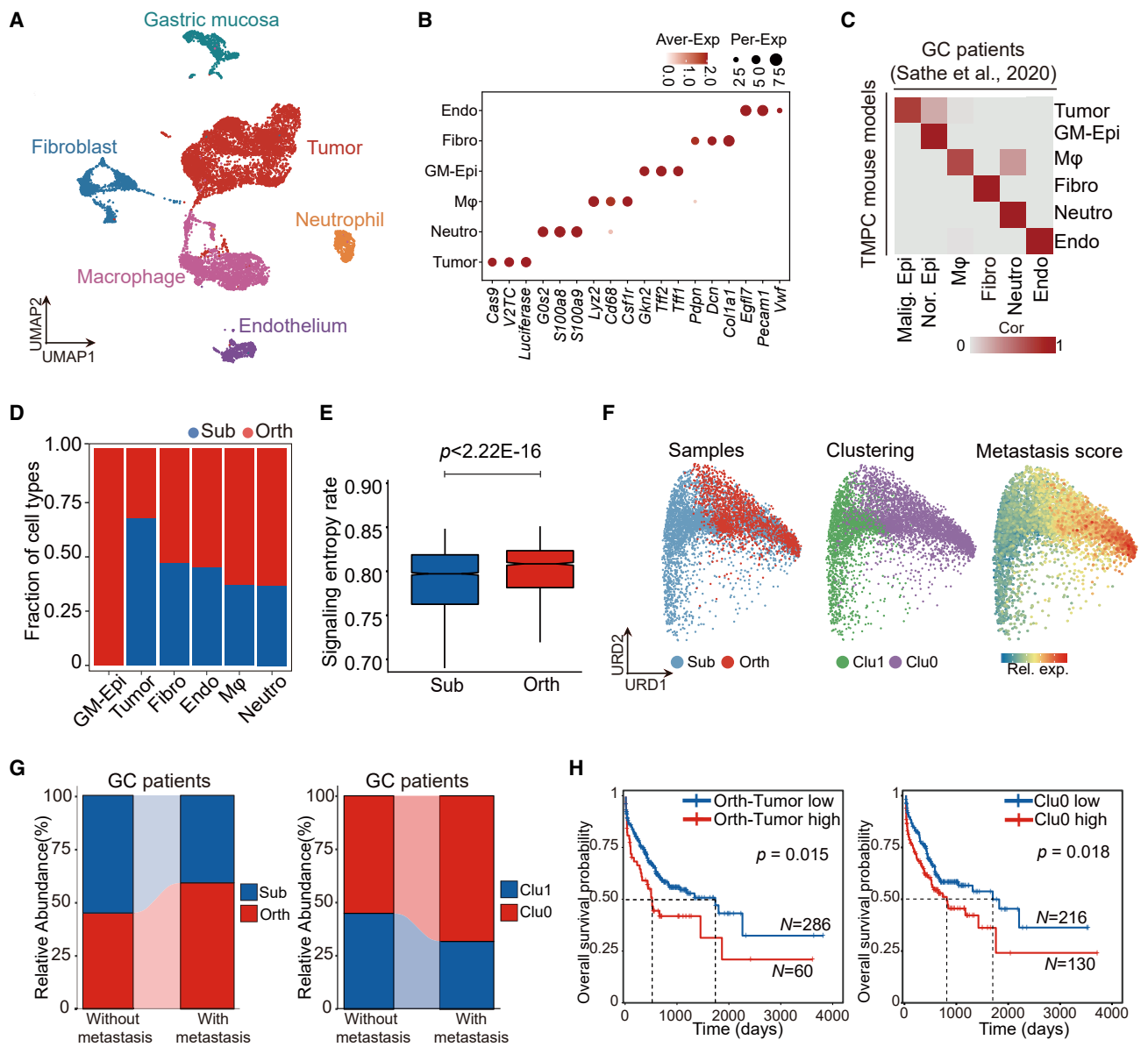
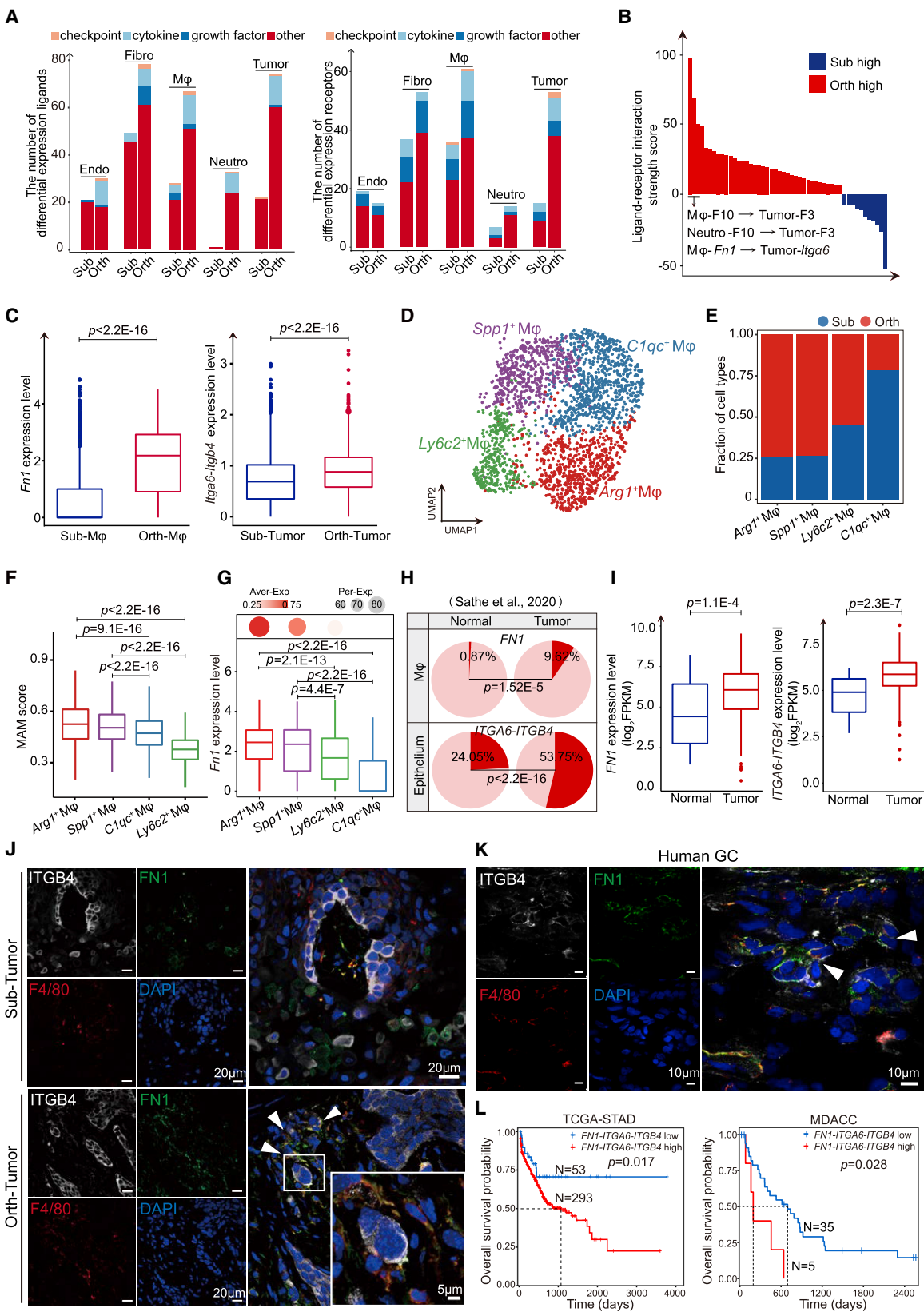


Figure 4. Single-cell transcriptome analyses reveal the cellular and molecular differences between the subcutaneous and orthotopic TMPC tumors

- (A) The UMAP plot of the subcutaneous and orthotopic TMPC tumors showing different cell types.
- (B) The dot plot showing the expression levels of marker genes for each cell type.
- (C) The heatmap showing the correlations between the indicated mouse cell types and human GC cell types annotated by singleR. The scRNA-seq data of GC patients were analyzed from <https://dna-discovery.stanford.edu>.
- (D) The proportion of each cell type in the subcutaneous and orthotopic tumors.
- (E) The boxplot showing the signaling entropy levels of subcutaneous and orthotopic tumor cells. Statistical significance was determined by Wilcoxon rank-sum test.
- (F) The URD maps of tumor cells from the subcutaneous and orthotopic TMPC tumors. The dots were colored by sample origins (left), unsupervised clustering (middle), and the expression level of metastasis scores (right), which derived from significantly highly expressed genes of GC patients with metastasis, comparing with those without metastasis in the TCGA-STAD cohort.
- (G) The alluvial plots showing the composition variation of two molecular subtypes of GC patients with or without metastasis in the TCGA-STAD cohort. The feature genes were derived from the signature genes of the subcutaneous and orthotopic tumor cells (left) or the clu0 and clu1 tumor cells (right).
- (H) The Kaplan-Meier survival curves of TCGA-STAD patients with low and high expression levels of orthotopic tumor cell signature genes (left) and clu0 signature genes (right). Statistical significance was determined by log rank test.



(legend on next page)

and the Wnt pathway (Figure S4D). Further, high expression levels of the orthotopic tumor signature genes were associated with poor prognosis of GC patients. And similarly, high expression levels of the cluster 0 signature genes were also associated with poor prognosis of GC patients (Figure 4H).

Further, fibroblasts in the orthotopic tumors expressed high levels of genes involved in positive regulation of angiogenesis, mesenchymal cell proliferation, and Wnt signaling pathway, compared with those in the subcutaneous tumors (Figure S4E). The high expression of orthotopic fibroblast gene signature predicted poor prognosis in GC patients (Figure S4F). However, gene signatures of neutrophils and endothelium did not show prognostic value (Figures S4G–S4J). Of note, the orthotopic macrophages expressed high levels of genes involved in inflammatory response, tissue remodeling, and extracellular structure organization (Figure S4K). Their gene signature was significantly associated with poor prognosis for GC patients (Figure S4L).

The interaction of *FN1*^{high} macrophages and *ITGA6*-*ITGB4*⁺ tumor cells is associated with GC malignancy and poor prognosis

To quantify the microenvironment complexity, we compared the numbers of differential expression ligands and receptors between subcutaneous and orthotopic tumors. In total, there were 282 significantly upregulated and 121 downregulated ligand genes in orthotopic tumors compared with subcutaneous ones (Figure 5A; Table S5). And 196 and 114 receptor genes were significantly up- and downregulated, respectively, in the orthotopic tumors compared with subcutaneous ones (Figure 5A; Table S5). iTALK cell-cell interaction analyses demonstrated that the cell-cell interaction complexity was dramatically increased in orthotopic tumors (Figure S5A; Table S5). *Fn1* was one of the most differentially expressed ligands between subcutaneous and orthotopic macrophages (Figures 5B and S5B; Table S5). Integrin α 6 could form a heterodimer with β 4, and their high expressions were associated with metastasis in various hu-

man cancers (Kariya et al., 2017). *Itga6* and *Itgb4* were among the top receptors highly expressed in the tumor cells, compared with non-tumor cells (Figure S5C; Table S5). And orthotopic macrophages and tumor cells expressed significantly higher levels of *Fn1*, *Itga6*, and *Itgb4* than the subcutaneous ones, respectively (Figure 5C).

The tumor-associated macrophages (TAMs) in GC could be divided into four subpopulations on the Uniform Manifold Approximation and Projection (UMAP), with specific markers, *C1qc*, *Arg1*, *Spp1*, and *Ly6c2*, respectively (Figures 5D and S5D; Table S4). There were more *C1qc*⁺ TAMs in the subcutaneous tumors while more *Arg1*⁺ and *Spp1*⁺ TAMs in the orthotopic tumors (Figures 5E and S5E; Table S4). *C1qc*⁺ TAMs displayed M1 features with anti-tumor capacity, indicated by increased phagocytosis score and decreased angiogenesis score. Instead, the *Arg1*⁺ and *Spp1*⁺ TAMs were M2-like with high angiogenesis scores and low phagocytosis scores (Figures S5F and S5G; Table S3). Moreover, *Arg1*⁺ and *Spp1*⁺ TAMs also expressed high levels of metastasis-associated macrophage (MAM) gene signatures, compared with *C1qc*⁺ and *Ly6c2*⁺ TAMs (Figure 5F; Table S3) (Nieto et al., 2021; Zhang et al., 2020). *Fn1* was preferentially expressed in the metastasis-associated *Arg1*⁺ and *Spp1*⁺ macrophage subpopulations (Figure 5G; Table S4). In patients, 9.62% of TAMs expressed *Fn1*, while only 0.87% of macrophages could be detected with *Fn1* expression from the normal tissues. Meanwhile, 24.05% of normal gastric epithelial cells expressed *ITGA6*-*ITGB4* and 53.75% of GC tumor cells in contrast, measured by 10x Genomics scRNA-seq analyses of seven GC patients and their paired normal tissues (Sathe et al., 2020) (Figure 5H). Consistently, in the TCGA-STAD cohort, the expression levels of *Fn1* and *ITGA6*-*ITGB4* in gastric tumors were both significantly higher than those in the adjacent normal tissues (Figure 5I).

To visualize the integrin-fibronectin interaction between tumor cells and macrophages, we performed immunofluorescent staining of the subcutaneous and orthotopic tumors with antibodies against *ITGB4*, fibronectin 1, and F4/80, a marker for

Figure 5. The interaction between macrophages and tumor cells through *FN1* and integrin α 6 β 4 is associated with metastasis of orthotopic GC

- (A) The bar plots showing the number of differential expression ligands (left) and receptors (right) between subcutaneous and orthotopic subpopulations.
- (B) The bar plot showing the relative ligand-receptor interaction strength scores from microenvironment cells to tumor cells in the subcutaneous and orthotopic tumors.
- (C) The boxplots showing the expression levels of *Fn1* and *Itga6*-*Itgb4* between subcutaneous and orthotopic macrophages (left) and tumor cells (right), respectively. Two-tailed Wilcoxon's rank-sum tests were used to determine the significance levels.
- (D) The UMAP plot showing four subpopulations of macrophages in the subcutaneous and orthotopic TMPC tumors.
- (E) The proportion of each macrophage subpopulation in the subcutaneous and orthotopic tumors.
- (F) The expression levels of the MAM (metastasis-associated macrophage) signature genes in four subpopulations of macrophages. Two-tailed Wilcoxon's rank-sum tests were used to determine the significance levels.
- (G) The relative *Fn1* expression levels in four macrophage subpopulations. Statistical significance was determined by Wilcoxon rank-sum test.
- (H) The pie charts showing the ratios of *FN1*⁺ (top) and *ITGA6*-*ITGB4*⁺ (bottom) macrophages and epithelial cells in normal and malignant tissues from GC patients. Statistical significance was determined by Chi-squared test.
- (I) *FN1* (left) and *ITGA6*-*ITGB4* (right) expression levels of normal and tumor samples in the TCGA-STAD cohort. Statistical significance was determined by Wilcoxon rank-sum test.
- (J) Representative *ITGB4* (white), *FN1* (green), and F4/80 (red) staining of the subcutaneous and orthotopic TMPC tumors. Scale bar, 20 μ m. Box areas showing higher magnifications. Scale bar, 5 μ m. Arrowheads indicate the interactions between *FN1*^{high} macrophages and *ITGB4*⁺ tumor cells.
- (K) Representative *ITGB4* (white), *FN1* (green), and F4/80 (red) staining of tumors from the gastric cancer patient. Scale bar, 10 μ m. Arrowheads indicate the interactions between *FN1*^{high} macrophages and *ITGB4*⁺ tumor cells.
- (L) The Kaplan-Meier survival curves of GC patients with low and high expression levels of *FN1*-*ITGA6*-*ITGB4* in the TCGA-STAD (left) and MDACC (right) cohorts. Statistical significance was determined by log rank test.

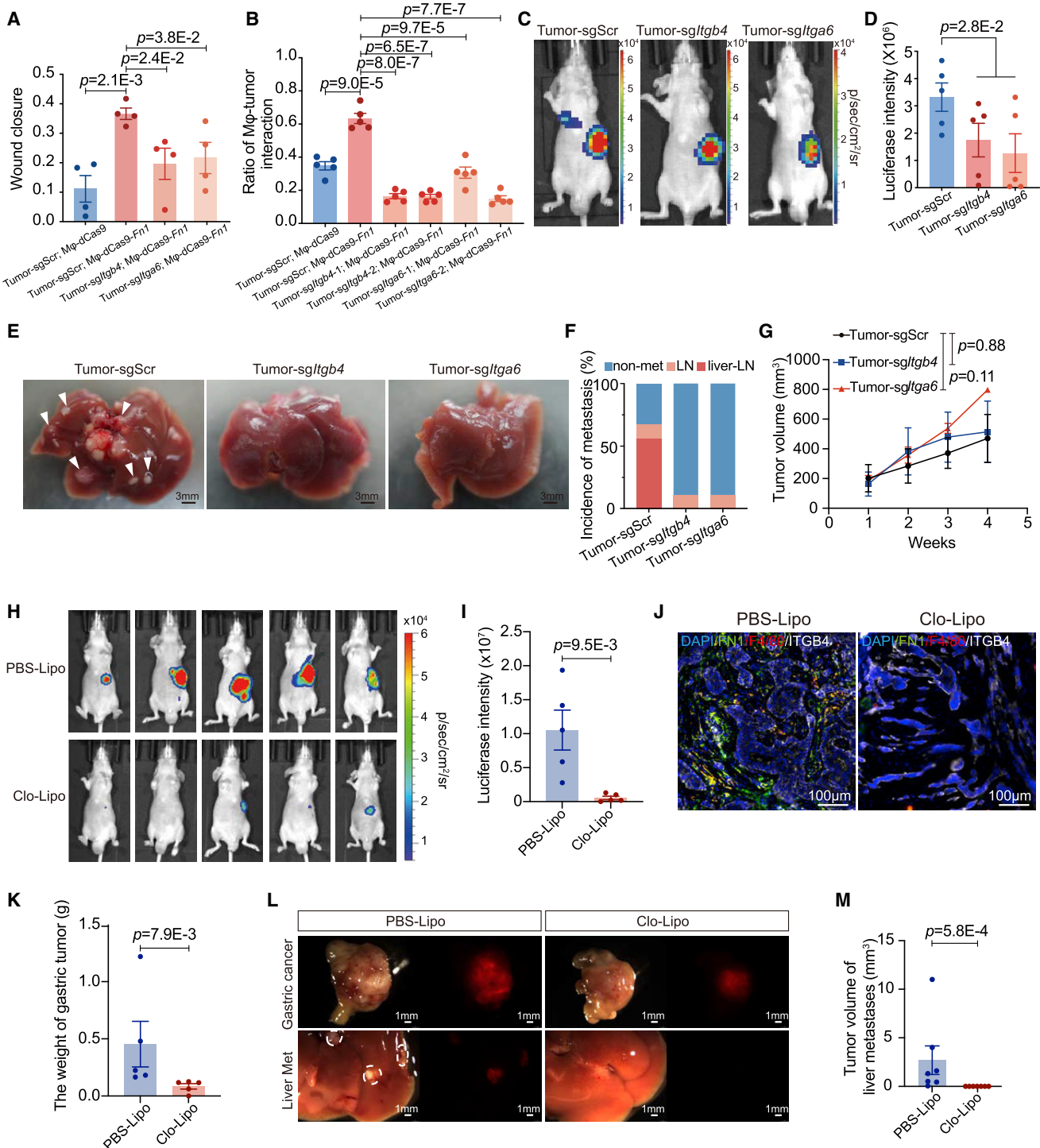


Figure 6. Macrophages promote the metastasis of orthotopic GC through the FN1-integrin $\alpha 6\beta 4$ interaction

(A) The bar plot showing the wound closure score in TMPC tumor cells with sgScr, sgltgb4, or sgltga6 co-cultured with RAW264.7 cells with or without dCas9-Fn1 (M_φ-dCas9-Fn1 or M_φ-dCas9, n = 4). Data presented as the means \pm the SEM; p value was calculated by unpaired t test.

(B) Ratio of M_φ-dCas9 or M_φ-dCas9-Fn1 adhering to the orthotopic TMPC tumor cells with sgScr, sgltgb4, or sgltga6 (n = 5). Data presented as the means \pm the SEM; p value was calculated by unpaired t test.

(C) Representative bioluminescent images of mice with orthotopic TMPC tumors sgScr, sgltgb4, or sgltga6.

(D) The luciferase fluorescence signal intensity of mice with orthotopic TMPC tumors sgScr, sgltgb4, or sgltga6 (n = 5). Data presented as the means \pm the SEM; p value was calculated by unpaired t test.

(legend continued on next page)

macrophage. FN1^{high} macrophages were close to or directly interacted with ITGB4⁺ tumor cells in the orthotopic tumors, but few of them did in the subcutaneous tumors (Figures 5J and S5H). Similarly, we also observed direct contact between the ITGB4⁺ tumor cells and FN1^{high} macrophages in human GC tissues (Figure 5K). With sorted TAMs from subcutaneous and orthotopic tumors, we found that more TAMs from the orthotopic tumors but not those from the subcutaneous tumors could bind with the tumor cells on the dish (Figure S5I). GC patients with high expression levels of FN1-ITGA6-ITGB4 have significantly decreased overall survival compared with those with low expression levels (Figure 5L). Further, GC patients with high expression levels of FN1-ITGA6-ITGB4 had significantly positive enrichments of EMT and TGF- β signaling pathways, compared with those with low expressions (Figure S5J). Taken together, these data suggested a critical role of the interaction of FN1 on macrophages with integrin α 6 β 4 on tumor cells in the malignancy and metastasis of GC.

The FN1-integrin α 6 β 4 interaction between tumor cells and macrophages is required for GC metastasis

To explore the functions of *Itga6* and *Itgb4* on GC metastasis, we cultured TMPC organoids with sgScr, sgltgb4, or sgltga6. *Itgb4* and *Itga6* loss significantly reduced the protrusion numbers of tumor organoids (Figures S6A and S6B). Then we performed a scratch assay of the TMPC tumor cells co-culturing with RAW 264.7 cells, an immortalized mouse macrophage cell line (Figure S6C). *Fn1* was upregulated in RAW 264.7 cells by CRISPRa (Figure S6D). We found that upregulating *Fn1* in RAW 264.7 cells significantly increased the migration of the TMPC cells. And further, disruption of either *Itga6* or *Itgb4* largely diminished the effect of *Fn1* upregulation on the migration of tumor cells (Figure 6A and S6E). Meanwhile, there was no significant difference in the migration ability between TMPC tumor-sgltgb4 or sgltga6 cells and TMPC tumor-sgScr cells (Figures S6F and S6G). And upregulation of *Fn1* in the RAW 264.7 cells significantly increased their direct binding with tumor cells. And either *Itga6* or *Itgb4* loss in the tumor cells significantly reduced their interaction with the RAW 264.7 cells (Figures 6B and S6C).

Then we tested the functions of integrin α 6 β 4 on GC progression *in vivo*. sgltga6 and sgltgb4 TMPC cells were orthotopically

transplanted into the stomach of recipients, with sgScr cells as control. The results showed that sgltga6 and sgltgb4 tumors grew significantly slower than the control TMPC tumors, measured by luciferase intensity and the tumor size (Figures 6C, 6D, S6H, and S6I). Further, five out of nine recipient mice with sgScr TMPC tumors had visible metastasis loci on both liver and lymph nodes, and one had only metastasis on the lymph node, while, in contrast, only one out of nine recipients with sgltga6 tumors had metastasis on lymph nodes, while none of them had liver metastasis. And similarly, only one out of nine recipients with sgltgb4 tumors had metastasis on lymph nodes (Figures 6E, 6F, S6J, and S6K). Of note, once subcutaneously transplanted into recipients, the growth of sgltga6 and sgltgb4 tumors was similar to the control TMPC tumors (Figure 6G). These data suggested that integrin α 6 β 4 had an orthotopically specific function on the progress of GC.

To verify the role of macrophages on tumor progression, we directly tested the potential functional roles of macrophages in mice with orthotopic tumors by clodronate liposome (Clo-Lipo) treatment. Mice with orthotopic TMPC tumors were treated with Clo-Lipo weekly by tail vein injection. The progress of the tumors was monitored by luciferase living imaging. The results showed that Clo-Lipo treatment significantly reduced the luciferase intensity, suggesting delayed tumor progression (Figures 6H and 6I). After 3 weeks of Clo-Lipo treatment, TMPC mice were sacrificed, and the tumors were analyzed. Clo-Lipo treatment successfully depleted macrophages in the orthotopic tumor tissues, indicated by flow cytometry (Figure S6L). And immunofluorescence staining confirmed that macrophages were significantly reduced in these orthotopic tumors with Clo-Lipo treatment (Figure 6J). The weight of gastric tumors in Clo-Lipo-treated mice was significantly lower than those in PBS-treated mice, suggesting that macrophages were essential for the growth of the primary orthotopic tumors (Figure 6K). Further, the liver metastasis was completely invisible in the Clo-Lipo-treated mice (Figures 6L and 6M). Taken together, these data indicated that macrophages played a vital role during orthotopic GC progression. These results strongly suggested that the interaction between integrin α 6 β 4 complex on tumors and upregulating FN1 on macrophages played a critical role in the GC progression, which was mediated by the microenvironment in the stomach.

(E) Representative bright-field images of livers from mice with orthotopic TMPC tumors sgScr, sgltgb4, or sgltga6. Arrowheads indicate the metastasis loci. Scale bar, 3 mm.

(F) The percentages of mice with orthotopic TMPC tumors sgScr, sgltgb4, or sgltga6 showing visible liver and lymph node metastases ($n = 9$).

(G) The growth curve of subcutaneous TMPC tumors with sgScr, sgltgb4, or sgltga6 ($n = 3$). Data presented as the means \pm the SEM; p value was calculated by unpaired t test.

(H) Bioluminescent images of orthotopic TMPC mice in PBS-Lipo- or Clo-Lipo-treated groups after 3 weeks of transplantation ($n = 5$).

(I) Quantification of bioluminescent intensity from orthotopic TMPC mice injected with PBS-Lipo or Clo-Lipo ($n = 5$). Data presented as the means \pm the SEM; p value was calculated by unpaired t test.

(J) Representative immunofluorescence staining images of ITGB4 (white), FN1 (green), and F4/80 (red) of tumors from orthotopic TMPC mice injected with PBS-Lipo or Clo-Lipo. Scale bar, 100 μ m.

(K) The weight of gastric tumors from orthotopic TMPC mice injected with PBS-Lipo or Clo-Lipo ($n = 5$). Data presented as the means \pm the SEM; p value was calculated by two-tailed Mann Whitney test.

(L) Representative bright-field (left) and red fluorescence (right) images of gastric tumors (top) and liver metastases (bottom) from orthotopic TMPC mice injected with PBS-Lipo or Clo-Lipo. Scale bar, 1 mm.

(M) The volumes of liver metastases from orthotopic TMPC mice injected with PBS-Lipo or Clo-Lipo ($n = 5$). Data presented as the means \pm the SEM; p value was calculated by two-tailed Mann Whitney test.

DISCUSSION

Despite GC being one of the most common and lethal human cancers, our understanding of the mechanisms for its initiation and progression remains very limited. One of the major obstacles might be the lack of proper animal models that would represent the multiple stages of this disease. The majority of current GC animal models need chemical carcinogen treatment to initiate or accelerate tumorigenesis, which is notoriously unstable and unclear on molecular mechanisms. Though several genetically engineered mouse models (GEMMs) of GC have been reported, few of them can fully recapitulate the whole process of GC in patients, especially distal metastasis (Sethi et al., 2020). Here, we report a new strategy to create genetics-defined *in vivo* (both subcutaneous and, importantly, *in situ*) GC models in mice, which represent the pathologies of GC at different stages, from dysplasia to full-blown carcinoma with distal metastasis. With this approach, any GC-associated genetic abnormality can be introduced into gastric organoids by CRISPR-Cas9 genome editing, shRNA, or other techniques. Once subcutaneously or orthotopically transplanted into recipient animals, these organoids would be transformed into GC through a process similar to that in patients. The resulting tumors are defined by drivers. Remarkably, this approach is very convenient and timesaving, compared with other strategies including GEMMs. Similar approaches have been applied to model lung cancers, colon-rectal cancer, breast cancer, prostate cancer, and others (Artegiani et al., 2019; Boj et al., 2015; Dekkers et al., 2020; Duarte et al., 2018; Lo et al., 2020; Matano et al., 2015; Na et al., 2022; Nanki et al., 2018; O'Rourke et al., 2017; Pan et al., 2022; Roper et al., 2017; Takeda et al., 2019; Wang et al., 2022). A recent study introduced TP53 and ARID1A mutations into human gastric organoids and generated subcutaneous malignancy in immune-deficient recipient mice (Lo et al., 2021). These studies, including ours, demonstrate that transplanting premalignant organoids with cancer-associated mutations into recipients would be a powerful and general strategy to model various types of human cancers, which would be of value to investigate the molecular and cellular mechanisms of tumorigenesis and to identify therapeutic targets and drugs.

A multistage transforming process has been generally proposed to human cancer. But little direct evidence has been provided to confirm this hypothesis, except for colorectal cancers (Artegiani et al., 2019; Vogelstein et al., 2013). About 30 years ago, Dr. Correa proposed that “human gastric carcinogenesis is a multistep and multifactorial process” (Correa, 1992). However, despite the clinical observations on these premalignant and malignant stages, there has been a significant lack of models that could stepwise represent the multistep process of gastric carcinogenesis. In this study, we apply the new strategy to create a series of GC models, which precisely recapitulate the stages of dysplasia, well-differentiated, poorly differentiated carcinoma, and metastatic adenocarcinoma, which help dissect the underlying driving factors, including both the genetic and microenvironmental factors. Thus, we establish a stepwise tumorigenesis model for GC, including that (1) TP53 loss and MYC overexpression initiate the process to form dysplasia, (2) PTEN loss fully transforms these dysplastic cells into low-grade

adenocarcinoma, (3) CDKN2B loss deteriorates this disease into poorly differentiated cancer, and finally (4) the microenvironmental factors, especially *FN1*^{high} TAMs, drive its distal metastases. Our work provides experimental evidence for the long proposed stepwise gastric tumorigenesis (Correa, 1992). Compared with the classic colorectal cancer model, which emphasizes only genetic mutations, we show that both the genetic factors and tumor microenvironmental factors contribute to the progress of GC. We propose that the initial genetic drivers play significant roles at the early stages, while the microenvironmental factors might be critical for its aggressiveness at the later stages. However, given the multiple subtypes of human GC with distinct mutations and clinical pathology (Cancer Genome Atlas Research, 2014), future studies need to test whether tumorigenesis of all of these GCs might follow this proposed model here. And further, the potential functions of the numerous other GC-associated mutations and various other microenvironmental factors in each step of GC tumorigenesis need to be dissected.

The significant effect of the microenvironment on tumorigenesis has been well recognized. However, due to its complexity, dissecting the specific microenvironmental factors and the underlying mechanisms has been a daunting task. Based on our surprising observation that the subcutaneous and orthotopic tumors with the same genetic drivers display dramatic differences in their metastatic capacities and single-cell analyses of interactomes, we propose that the stomach-specific macrophages promote metastases through the integrin-fibronectin interaction. TAMs can be divided into the M1 and M2 subpopulations according to their molecular features and functions in cancer (Mills et al., 2000). Among the protumor M2 macrophages, MAMs have been proposed, which express high levels of DAB2 and promote metastasis through secreting CSF1 and CCL2 (Marigo et al., 2020; Qian et al., 2011; Qian and Pollard, 2010). Our study with Clo-Lipo indicates that TAMs are critical for GC progression. Further, we showed that at least some of these macrophages could directly bind with cancer cells through the integrin-fibronectin interaction. Upregulating *Fn1* in macrophages increases the migration of co-cultured tumor cells, which can be blocked by the disruption of the integrin α6β4 complex. Depleting TAMs or disrupting the integrin-fibronectin interaction significantly repressed the progression of orthotopic tumors, but not the subcutaneous ones. Concordantly, there is emerging evidence suggesting that macrophages and other types of immune cells can directly couple with cancer cells at multiple stages of tumor progression, which need further investigation.

Limitations of the study

Despite that TP53, PTEN, CDKN2B, and MYC are frequently altered in human GCs and abnormalities of all these genes also happen in about 9% patients, there are plenty of other genes, such as ARID1A, CDH1, and FAT1/2/3/4, involved in GC. Whether and how these genes also play significant roles in GC tumorigenesis need further investigations. Specifically, our study suggests that TP53, MYC, PTEN, and CDKN2B alterations might function at different stages of GC tumorigenesis. However, additional studies with large-scale GC cohorts of different stages would be necessary to verify this conclusion.

STAR★METHODS

Detailed methods are provided in the online version of this paper and include the following:

- **KEY RESOURCES TABLE**
- **RESOURCE AVAILABILITY**
 - Lead contact
 - Materials availability
 - Data and code availability
- **EXPERIMENTAL MODELS AND SUBJECTS DETAILS**
 - Mice
- **METHOD DETAILS**
 - Organoid culture
 - Organoid genome editing
 - Organoid proliferation assay
 - Antibodies
 - Western blotting
 - Mouse model establishment
 - H&E, immunohistochemistry and immunofluorescence staining
 - CRISPRa system
 - RNA extraction and RT-qPCR
 - Wound-healing assay
 - Tumor-macrophage co-culture assay
 - Macrophages depletion *in vivo*
 - Flow cytometry
 - RNA-seq analyses
 - scRNA-seq analyses
 - Cell-cell interaction analyses
 - Clinical correlation analyses
 - Survival analyses
- **QUANTIFICATION AND STATISTICAL ANALYSIS**

SUPPLEMENTAL INFORMATION

Supplemental information can be found online at <https://doi.org/10.1016/j.celrep.2022.111482>.

ACKNOWLEDGMENTS

We thank Dr. Yuquan Wei for generous support. We thank all the CC-LY lab members for discussion and technical support. We thank the Core Facilities of West China Hospital and the Chengdu OrganoidMed Medical Laboratory for technical support. This work was supported by the National Natural Science Foundation of China (82130007, 82170171, 81770157), the Sichuan Science and Technology Program (2020YFQ0059, 2018JZ0077, 2017TJPT0005), and 1.3.5. Project for Disciplines of Excellence, West China Hospital, Sichuan University (ZYJC21009 and ZYYC20004).

AUTHOR CONTRIBUTIONS

Conceptualization, C.C.; methodology: Z.L., A.Z., H.L., M.Z., X.C., X.P., M.W., X.D., L.G., L.Z., J.W., Y.Y., Q.Z., B.W., J.Z., Y.W., X.S., K.L., W.Z., X.C., K.Y., and X.C.; investigation: Z.L., A.Z., H.L., M.Z., X.C., X.P., M.W., X.D., L.G., L.Z., J.W., Y.Y., Q.Z., B.W., J.Z., Y.W., X.S., K.L., W.Z., X.C., K.Y., and X.C.; resources: Y.Z., C.Z., Y.W., L.C., and Z.Z.; writing-original draft: Z.L., A.Z., H.L., M.Z., X.C., X.P., M.W., L.G., J.H., Y.L., and C.C.; writing-review & editing: Z.L., A.Z., H.L., M.Z., X.C., X.P., M.W., L.G., J.H., Y.L., and C.C.; funding acquisition: Y.L. and C.C.; supervision: Z.Z., J.H., Y.L., and C.C.

DECLARATION OF INTERESTS

The authors declare no competing interests.

Received: January 17, 2022

Revised: July 21, 2022

Accepted: September 19, 2022

Published: October 18, 2022

REFERENCES

- Alonso-Curbelo, D., Ho, Y.J., Burdziak, C., Maag, J.L.V., Morris, J.P., 4th, Chandwani, R., Chen, H.A., Tsanov, K.M., Barriga, F.M., Luan, W., et al. (2021). A gene-environment-induced epigenetic program initiates tumorigenesis. *Nature* 590, 642–648. <https://doi.org/10.1038/s41586-020-03147-x>.
- Anderson, N.M., and Simon, M.C. (2020). The tumor microenvironment. *Curr. Biol.* 30, R921–R925. <https://doi.org/10.1016/j.cub.2020.06.081>.
- Aran, D., Looney, A.P., Liu, L., Wu, E., Fong, V., Hsu, A., Chak, S., Naikawadi, R.P., Wolters, P.J., Abate, A.R., et al. (2019). Reference-based analysis of lung single-cell sequencing reveals a transitional profibrotic macrophage. *Nat. Immunol.* 20, 163–172. <https://doi.org/10.1038/s41590-018-0276-y>.
- Artegiani, B., van Voorthuijsen, L., Lindeboom, R.G.H., Seinstra, D., Heo, I., Tapia, P., López-Iglesias, C., Postrach, D., Dayton, T., Oka, R., et al. (2019). Probing the tumor suppressor function of BAP1 in CRISPR-engineered human liver organoids. *Cell Stem Cell* 24, 927–943.e6. <https://doi.org/10.1016/j.stem.2019.04.017>.
- Barker, N., Huch, M., Kujala, P., van de Wetering, M., Snippert, H.J., van Es, J.H., Sato, T., Stange, D.E., Begthel, H., van den Born, M., et al. (2010). Lgr5(+ve) stem cells drive self-renewal in the stomach and build long-lived gastric units *in vitro*. *Cell Stem Cell* 6, 25–36. <https://doi.org/10.1016/j.stem.2009.11.013>.
- Birkman, E.M., Mansuri, N., Kurki, S., Ålgars, A., Lintunen, M., Ristamäki, R., Sundström, J., and Carpén, O. (2018). Gastric cancer: immunohistochemical classification of molecular subtypes and their association with clinicopathological characteristics. *Virchows Arch.* 472, 369–382. <https://doi.org/10.1007/s00428-017-2240-x>.
- Boj, S.F., Hwang, C.I., Baker, L.A., Chio, I.I.C., Engle, D.D., Corbo, V., Jager, M., Ponz-Sarvise, M., Tiriac, H., Spector, M.S., et al. (2015). Organoid models of human and mouse ductal pancreatic cancer. *Cell* 160, 324–338. <https://doi.org/10.1016/j.cell.2014.12.021>.
- Broutier, L., Mastrogiovanni, G., Versteegen, M.M., Frances, H.E., Gavarró, L.M., Bradshaw, C.R., Allen, G.E., Arnes-Benito, R., Sidorova, O., Gaspersz, M.P., et al. (2017). Human primary liver cancer-derived organoid cultures for disease modeling and drug screening. *Nat. Med.* 23, 1424–1435. <https://doi.org/10.1038/nm.4438>.
- Cancer Genome Atlas Research Network (2014). Comprehensive molecular characterization of gastric adenocarcinoma. *Nature* 513, 202–209. <https://doi.org/10.1038/nature13480>.
- Chavez, A., Scheiman, J., Vora, S., Pruitt, B.W., Tuttle, M., P R Iyer, E., Lin, S., Kiani, S., Guzman, C.D., Wiegand, D.J., et al. (2015). Highly efficient Cas9-mediated transcriptional programming. *Nat. Methods* 12, 326–328. <https://doi.org/10.1038/nmeth.3312>.
- Chen, X., and Song, E. (2022). The theory of tumor ecosystem. *Cancer Commun.* 42, 587–608. <https://doi.org/10.1002/cac2.12316>.
- Cooper, G.M. (2000). *The Cell : A Molecular Approach*, 2nd edition (ASM Press; Sinauer Associates).
- Correa, P. (1992). Human gastric carcinogenesis: a multistep and multifactorial process—first American cancer society award lecture on cancer epidemiology and prevention. *Cancer Res.* 52, 6735–6740.
- Cristescu, R., Lee, J., Nebozhyn, M., Kim, K.M., Ting, J.C., Wong, S.S., Liu, J., Yue, Y.G., Wang, J., Yu, K., et al. (2015). Molecular analysis of gastric cancer identifies subtypes associated with distinct clinical outcomes. *Nat. Med.* 21, 449–456. <https://doi.org/10.1038/nm.3850>.

- Dekkers, J.F., Whittle, J.R., Vaillant, F., Chen, H.R., Dawson, C., Liu, K., Geurts, M.H., Herold, M.J., Clevers, H., Lindeman, G.J., and Visvader, J.E. (2020). Modeling breast cancer using CRISPR-cas9-mediated engineering of human breast organoids. *J. Natl. Cancer Inst.* 112, 540–544. <https://doi.org/10.1093/jnci/djz196>.
- Dobin, A., Davis, C.A., Schlesinger, F., Drenkow, J., Zaleski, C., Jha, S., Batut, P., Chaisson, M., and Gingeras, T.R. (2013). STAR: ultrafast universal RNA-seq aligner. *Bioinformatics* 29, 15–21. <https://doi.org/10.1093/bioinformatics/bts635>.
- Duarte, A.A., Gogola, E., Sachs, N., Barazas, M., Annunziato, S., R de Ruiter, J., Velds, A., Blatter, S., Houthuijzen, J.M., van de Ven, M., et al. (2018). BRCA-deficient mouse mammary tumor organoids to study cancer-drug resistance. *Nat. Methods* 15, 134–140. <https://doi.org/10.1038/nmeth.4535>.
- Farrell, J.A., Wang, Y., Riesenfeld, S.J., Shekhar, K., Regev, A., and Schier, A.F. (2018). Single-cell reconstruction of developmental trajectories during zebrafish embryogenesis. *Science* 360, eaar3131. <https://doi.org/10.1126/science.aar3131>.
- Fearon, E.R., and Vogelstein, B. (1990). A genetic model for colorectal tumorigenesis. *Cell* 61, 759–767. [https://doi.org/10.1016/0092-8674\(90\)90186-i](https://doi.org/10.1016/0092-8674(90)90186-i).
- Hang, X., Zhao, L., Wu, B., Li, S., Liu, P., Xu, J., Wang, X., Chi, P., Chen, C., Niu, T., et al. (2022). BCL-2 isoform beta promotes angiogenesis by TRiC-mediated upregulation of VEGF-A in lymphoma. *Oncogene* 41, 3655–3663. <https://doi.org/10.1038/s41388-022-02372-0>.
- Hänzelmann, S., Castelo, R., and Guinney, J. (2013). GSVA: gene set variation analysis for microarray and RNA-seq data. *BMC Bioinf.* 14, 7. <https://doi.org/10.1186/1471-2105-14-7>.
- He, Y., Wang, Y., Luan, F., Yu, Z., Feng, H., Chen, B., and Chen, W. (2021). Chinese and global burdens of gastric cancer from 1990 to 2019. *Cancer Med.* 10, 3461–3473. <https://doi.org/10.1002/cam4.3892>.
- Kariya, Y., Kariya, Y., and Gu, J. (2017). Roles of integrin alpha6beta4 glycosylation in cancer. *Cancers (Basel)* 9 (7), 79.
- Ko, G.H., Go, S.I., Lee, W.S., Lee, J.H., Jeong, S.H., Lee, Y.J., Hong, S.C., and Ha, W.S. (2017). Prognostic impact of Ki-67 in patients with gastric cancer—the importance of depth of invasion and histologic differentiation. *Medicine (Baltimore)* 96, e7181. <https://doi.org/10.1097/MD.00000000000007181>.
- Li, H., Handsaker, B., Wysoker, A., Fennell, T., Ruan, J., Homer, N., Marth, G., Abecasis, G., and Durbin, R.; 1000 Genome Project Data Processing Subgroup (2009). The sequence alignment/map format and SAMtools. *Bioinformatics* 25, 2078–2079. <https://doi.org/10.1093/bioinformatics/btp352>.
- Li, X., Zhang, C., Gong, T., Ni, X., Li, J., Zhan, D., Liu, M., Song, L., Ding, C., Xu, J., et al. (2018). A time-resolved multi-omic atlas of the developing mouse stomach. *Nat. Commun.* 9, 4910. <https://doi.org/10.1038/s41467-018-07463-9>.
- Lo, Y.H., Karlsson, K., and Kuo, C.J. (2020). Applications of organoids for cancer biology and precision medicine. *Nat. Cancer* 1, 761–773. <https://doi.org/10.1038/s43018-020-0102-y>.
- Lo, Y.H., Kolahi, K.S., Du, Y., Chang, C.Y., Krokhutin, A., Nair, A., Sobba, W.D., Karlsson, K., Jones, S.J., Longacre, T.A., et al. (2021). A CRISPR/Cas9-Engineered ARID1A-deficient human gastric cancer organoid model reveals essential and nonessential modes of oncogenic transformation. *Cancer Discov.* 11, 1562–1581. <https://doi.org/10.1158/2159-8290.CD-20-1109>.
- Love, M.I., Huber, W., and Anders, S. (2014). Moderated estimation of fold change and dispersion for RNA-seq data with DESeq2. *Genome Biol.* 15, 550. <https://doi.org/10.1186/s13059-014-0550-8>.
- Marigo, I., Trovato, R., Hofer, F., Ingangi, V., Desantis, G., Leone, K., De Santis, F., Ugel, S., Cane, S., Simonelli, A., et al. (2020). Disabled homolog 2 controls prometastatic activity of tumor-associated macrophages. *Cancer Discov.* 10, 1758–1773. <https://doi.org/10.1158/2159-8290.CD-20-0036>.
- Matano, M., Date, S., Shimokawa, M., Takano, A., Fujii, M., Ohta, Y., Watanabe, T., Kanai, T., and Sato, T. (2015). Modeling colorectal cancer using CRISPR-Cas9-mediated engineering of human intestinal organoids. *Nat. Med.* 21, 256–262. <https://doi.org/10.1038/nm.3802>.
- Mills, C.D., Kincaid, K., Alt, J.M., Heilman, M.J., and Hill, A.M. (2000). M-1/M-2 macrophages and the Th1/Th2 paradigm. *J. Immunol.* 164, 6166–6173. <https://doi.org/10.4049/jimmunol.164.12.6166>.
- Na, F., Pan, X., Chen, J., Chen, X., Wang, M., Chi, P., You, L., Zhang, L., Zhong, A., Zhao, L., et al. (2022). KMT2C deficiency promotes small cell lung cancer metastasis through DNMT3A-mediated epigenetic reprogramming. *Nat. Cancer* 3, 753–767. <https://doi.org/10.1038/s43018-022-00361-6>.
- Nagaraja, A.K., Kikuchi, O., and Bass, A.J. (2019). Genomics and targeted therapies in gastroesophageal adenocarcinoma. *Cancer Discov.* 9, 1656–1672. <https://doi.org/10.1158/2159-8290.CD-19-0487>.
- Nanki, K., Toshimitsu, K., Takano, A., Fujii, M., Shimokawa, M., Ohta, Y., Matano, M., Seino, T., Nishikori, S., Ishikawa, K., et al. (2018). Divergent routes toward Wnt and R-spondin niche independency during human gastric carcinogenesis. *Cell* 174, 856–869.e17. <https://doi.org/10.1016/j.cell.2018.07.027>.
- O'Rourke, K.P., Loizou, E., Livshits, G., Schatoff, E.M., Baslan, T., Manchado, E., Simon, J., Romesser, P.B., Leach, B., Han, T., et al. (2017). Transplantation of engineered organoids enables rapid generation of metastatic mouse models of colorectal cancer. *Nat. Biotechnol.* 35, 577–582. <https://doi.org/10.1038/nbt.3837>.
- Nieto, P., Elosua-Bayes, M., Trincado, J.L., Marchese, D., Massoni-Badosa, R., Salvany, M., Henriques, A., Nieto, J., Aguilar-Fernández, S., Mereu, E., et al. (2021). A single-cell tumor immune atlas for precision oncology. *Genome Res* 31, 1913–1926.
- Oh, S.C., Sohn, B.H., Cheong, J.H., Kim, S.B., Lee, J.E., Park, K.C., Lee, S.H., Park, J.L., Park, Y.Y., Lee, H.S., et al. (2018). Clinical and genomic landscape of gastric cancer with a mesenchymal phenotype. *Nat. Commun.* 9, 1777. <https://doi.org/10.1038/s41467-018-04179-8>.
- Pan, X., Wang, J., Guo, L., Na, F., Du, J., Chen, X., Zhong, A., Zhao, L., Zhang, L., Zhang, M., et al. (2022). Identifying a confused cell identity for esophageal squamous cell carcinoma. *Signal Transduct. Target. Ther.* 7, 122. <https://doi.org/10.1038/s41392-022-00946-8>.
- Platt, R.J., Chen, S., Zhou, Y., Yim, M.J., Swiech, L., Kempton, H.R., Dahlman, J.E., Parnas, O., Eisenhaure, T.M., Jovanovic, M., et al. (2014). CRISPR-Cas9 knockin mice for genome editing and cancer modeling. *Cell* 159, 440–455. <https://doi.org/10.1016/j.cell.2014.09.014>.
- Pollard, J.W. (2004). Tumour-educated macrophages promote tumour progression and metastasis. *Nat. Rev. Cancer* 4, 71–78. <https://doi.org/10.1038/nrc1256>.
- Qian, B.Z., Li, J., Zhang, H., Kitamura, T., Zhang, J., Campion, L.R., Kaiser, E.A., Snyder, L.A., and Pollard, J.W. (2011). CCL2 recruits inflammatory monocytes to facilitate breast-tumour metastasis. *Nature* 475, 222–225. <https://doi.org/10.1038/nature10138>.
- Qian, B.Z., and Pollard, J.W. (2010). Macrophage diversity enhances tumor progression and metastasis. *Cell* 141, 39–51. <https://doi.org/10.1016/j.cell.2010.03.014>.
- Rhodes, D.R., Yu, J., Shanker, K., Deshpande, N., Varambally, R., Ghosh, D., Barrette, T., Pandey, A., and Chinnaian, A.M. (2004). Large-scale meta-analysis of cancer microarray data identifies common transcriptional profiles of neoplastic transformation and progression. *Proc. Natl. Acad. Sci. USA* 101, 9309–9314. <https://doi.org/10.1073/pnas.0401994101>.
- Roper, J., Tammela, T., Cetinbas, N.M., Akkad, A., Roghanian, A., Rickelt, S., Almeqdadi, M., Wu, K., Oberli, M.A., Sánchez-Rivera, F.J., et al. (2017). In vivo genome editing and organoid transplantation models of colorectal cancer and metastasis. *Nat. Biotechnol.* 35, 569–576. <https://doi.org/10.1038/nbt.3836>.
- Santos, C.P., Lapi, E., Martínez de Villarreal, J., Álvaro-Espínosa, L., Fernández-Barral, A., Barbáchan, A., Domínguez, O., Laughney, A.M., Megías, D., Muñoz, A., and Real, F.X. (2019). Urothelial organoids originating from Cd49f(high) mouse stem cells display Notch-dependent differentiation capacity. *Nat. Commun.* 10, 4407. <https://doi.org/10.1038/s41467-019-12307-1>.
- Sathe, A., Grimes, S.M., Lau, B.T., Chen, J., Suarez, C., Huang, R.J., Poultides, G., and Ji, H.P. (2020). Single-cell genomic characterization reveals the cellular reprogramming of the gastric tumor microenvironment. *Clin. Cancer Res.* 26, 2640–2653. <https://doi.org/10.1158/1078-0432.CCR-19-3231>.

- Schneider, C.A., Rasband, W.S., and Eliceiri, K.W. (2012). NIH Image to ImageJ: 25 years of image analysis. *Nat. Methods* 9, 671–675. <https://doi.org/10.1038/nmeth.2089>.
- Seidlitz, T., Chen, Y.T., Uhlemann, H., Schölch, S., Kochall, S., Merker, S.R., Klimova, A., Hennig, A., Schweitzer, C., Pape, K., et al. (2019). Mouse models of human gastric cancer subtypes with stomach-specific CreERT2-mediated pathway alterations. *Gastroenterology* 157, 1599–1614.e2. <https://doi.org/10.1053/j.gastro.2019.09.026>.
- Sethi, N.S., Kikuchi, O., Duronio, G.N., Stachler, M.D., McFarland, J.M., Ferer-Luna, R., Zhang, Y., Bao, C., Bronson, R., Patil, D., et al. (2020). Early TP53 alterations engage environmental exposures to promote gastric premalignancy in an integrative mouse model. *Nat. Genet.* 52, 219–230. <https://doi.org/10.1038/s41588-019-0574-9>.
- Stange, D.E., Koo, B.K., Huch, M., Sibbel, G., Basak, O., Lyubimova, A., Ku-jala, P., Bartfeld, S., Koster, J., Geahlen, J.H., et al. (2013). Differentiated Troy+ chief cells act as reserve stem cells to generate all lineages of the stomach epithelium. *Cell* 155, 357–368. <https://doi.org/10.1016/j.cell.2013.09.008>.
- Stuart, T., Butler, A., Hoffman, P., Hafemeister, C., Papalexi, E., Mauck, W.M., 3rd, Hao, Y., Stoeckius, M., Smibert, P., and Satija, R. (2019). Comprehensive integration of single-cell data. *Cell* 177, 1888–1902.e21. <https://doi.org/10.1016/j.cell.2019.05.031>.
- Subramanian, A., Tamayo, P., Mootha, V.K., Mukherjee, S., Ebert, B.L., Gillette, M.A., Paulovich, A., Pomeroy, S.L., Golub, T.R., Lander, E.S., and Mesirov, J.P. (2005). Gene set enrichment analysis: a knowledge-based approach for interpreting genome-wide expression profiles. *Proc. Natl. Acad. Sci. USA* 102, 15545–15550. <https://doi.org/10.1073/pnas.0506580102>.
- Sung, H., Ferlay, J., Siegel, R.L., Laversanne, M., Soerjomataram, I., Jemal, A., and Bray, F. (2021). Global cancer statistics 2020: GLOBOCAN estimates of incidence and mortality worldwide for 36 cancers in 185 countries. *CA. Cancer J. Clin.* 71, 209–249. <https://doi.org/10.3322/caac.21660>.
- Takeda, H., Kataoka, S., Nakayama, M., Ali, M.A.E., Oshima, H., Yamamoto, D., Park, J.W., Takegami, Y., An, T., Jenkins, N.A., et al. (2019). CRISPR-Cas9-mediated gene knockout in intestinal tumor organoids provides functional validation for colorectal cancer driver genes. *Proc. Natl. Acad. Sci. USA* 116, 15635–15644. <https://doi.org/10.1073/pnas.1904714116>.
- Till, J.E., Yoon, C., Kim, B.J., Roby, K., Addai, P., Jonokuchi, E., Tang, L.H., Yoon, S.S., and Ryeom, S. (2017). Oncogenic KRAS and p53 loss drive gastric tumorigenesis in mice that can be attenuated by E-cadherin expression. *Cancer Res.* 77, 5349–5359. <https://doi.org/10.1158/0008-5472.CAN-17-0061>.
- Vogelstein, B., Papadopoulos, N., Velculescu, V.E., Zhou, S., Diaz, L.A., Jr., and Kinzler, K.W. (2013). Cancer genome landscapes. *Science* 339, 1546–1558. <https://doi.org/10.1126/science.1235122>.
- Wang, K., Yuen, S.T., Xu, J., Lee, S.P., Yan, H.H.N., Shi, S.T., Siu, H.C., Deng, S., Chu, K.M., Law, S., et al. (2014). Whole-genome sequencing and comprehensive molecular profiling identify new driver mutations in gastric cancer. *Nat. Genet.* 46, 573–582. <https://doi.org/10.1038/ng.2983>.
- Wang, M., Chen, X., Tan, P., Wang, Y., Pan, X., Lin, T., Jiang, Y., Wang, B., Xu, H., Wang, Y., et al. (2022). Acquired semi-squamatization during chemotherapy suggests differentiation as a therapeutic strategy for bladder cancer. *Cancer Cell* 40, 1044–1059.e8. <https://doi.org/10.1016/j.ccr.2022.1008.1010>.
- Wang, Y., Wang, R., Zhang, S., Song, S., Jiang, C., Han, G., Wang, M., Ajani, J., Futreal, A., and Wang, L. (2019). iTALK: an R Package to characterize and illustrate intercellular communication. Preprint at bioRxiv. <https://doi.org/10.1101/507871>.
- Yang, D., Qu, F., Cai, H., Chuang, C.H., Lim, J.S., Jahchan, N., Grüner, B.M., S Kuo, C., Kong, C., Oudin, M.J., et al. (2019). Axon-like protrusions promote small cell lung cancer migration and metastasis. *eLife* 8, e50616. <https://doi.org/10.7554/eLife.50616>.
- Yang, L., Liu, Q., Zhang, X., Liu, X., Zhou, B., Chen, J., Huang, D., Li, J., Li, H., Chen, F., et al. (2020). DNA of neutrophil extracellular traps promotes cancer metastasis via CCDC25. *Nature* 583, 133–138. <https://doi.org/10.1038/s41586-020-2394-6>.
- Yeoh, K.G., and Tan, P. (2022). Mapping the genomic diaspora of gastric cancer. *Nat. Rev. Cancer* 22, 71–84. <https://doi.org/10.1038/s41568-021-00412-7>.
- Yu, G., Wang, L.G., Han, Y., and He, Q.Y. (2012). clusterProfiler: an R package for comparing biological themes among gene clusters. *OMICS* 16, 284–287. <https://doi.org/10.1089/omi.2011.0118>.
- Yu, S., Yang, M., and Nam, K.T. (2014). Mouse models of gastric carcinogenesis. *J. Gastric Cancer* 14, 67–86. <https://doi.org/10.5230/jgc.2014.14.2.67>.
- Zhang, L., Li, Z., Skrzypczynska, K.M., Fang, Q., Zhang, W., O'Brien, S.A., He, Y., Wang, L., Zhang, Q., Kim, A., et al. (2020). Single-cell analyses inform mechanisms of myeloid-targeted therapies in colon cancer. *Cell* 181, 442–459.e429.

STAR★METHODS

KEY RESOURCES TABLE

REAGENT or RESOURCE	SOURCE	IDENTIFIER
Antibodies		
Recombinant Anti-Ki67 antibody [SP6]	Abcam	Cat# ab16667; RRID: AB_302459
CDK4 Polyclonal antibody	Proteintech	Cat# 11026-1-AP; RRID: AB_2078702
Anti-Cytokeratin 7 antibody	Abcam	Cat# ab181598; RRID: AB_2783822
Cas9 (<i>S. pyogenes</i>) (E7M1H)	Cell Signaling Technology	Cat# 19526; RRID: AB_2798820
XP® Rabbit mAb		
Anti-beta Catenin antibody	Thermo Fisher Scientific	Cat# MA5-32540; RRID: AB_2809817
Anti-ErbB2/HER2 antibody	Abcam	Cat# ab134182; RRID: AB_2893179
Anti-EPCAM antibody	Abcam	Cat# ab213500; RRID: AB_2884975
Anti-GFP antibody	Abcam	Cat# ab290; RRID: AB_303395
Anti-Fibronectin antibody [IST-9] - BSA and Azide free	Abcam	Cat# ab6328; RRID: AB_30542
Anti-ITGB4 antibody	Novus biologicals	Cat# NBP2-38297
Anti-F4/80 antibody [Cl: A3-1] - Macrophage Marker	Abcam	Cat# ab6640; RRID: AB_1140040
Sox2 (D9B8N) Rabbit mAb	Cell Signaling Technology	Cat# 23064; RRID: AB_2714146
Anti-LGR5 Rabbit Polyclonal Antibody	OriGene	Cat# TA324287
PTEN (138G6) Rabbit	Cell Signaling Technology	Cat# 9559; RRID: AB_390810
Anti-c-Myc (phospho S62) antibody [EPR17924]	Abcam	Cat# ab185656
CD45	BioLegend	Cat#109820; RRID: AB_492872
CD11b	BioLegend	Cat#101216; RRID: AB_312799
F4/80	BioLegend	Cat#123132; RRID: AB_11203717
The sequences of sgRNAs used in this study		
Scramble	GACATTCTTCCCCACTGG	N/A
<i>Pten</i>	GGATCGTTAGCAGAAACAA	N/A
<i>Cdkn2b</i>	GTTGGCGGCAGCAGTGACG	N/A
<i>Itga6</i> sg1	GCCTGCTCTACCTGTCCGCG	N/A
<i>Itga6</i> sg2	CCGGATCACGTTGCTCTCGC	N/A
<i>Itgb4</i> sg1	CAGGGCCCTGTTGCAGCCA	N/A
<i>Itgb4</i> sg2	GCAGCAGCAGCTTCACCCAT	N/A
<i>Fn1</i>	GCCAATAGGCCGCGCGGTCCG	N/A
The sequences of primers used in this study		
Gene	Forward primer	Reverse primer
<i>Trp53</i> Common		TGGATGGTGGTATACTCAGAGC
<i>Trp53</i> mut	CAGCCTCTGTTCCACATACACT	N/A
<i>Trp53</i> Wild	AGGCTTAGAGGGTCAAGCTG	N/A
<i>Cas9</i> Wild	CTGGCTTCTGAGGACCG	N/A
<i>Cas9</i> Wild		AGCCTGCCAGAACAGACTCC
<i>Cas9</i> Mutant	CTCCGTCGTGGCCTTATAGT	N/A
<i>Cas9</i> Mutant		GCTAACCATGTTCATGCCCTC
<i>Pten</i>	GAGCCATTCCATCCTGCAG	CTAGCCGAACACTCCCTAGG
<i>Cdkn2b</i>	ACCGAAGCTACTGGGTCT	CTAGTGGCGAGGGATGTTTC
<i>Itga6</i>	CCTTGGAGAACGGATGTCTT	GTTTGTCCCTCGGCTCTC
<i>Itgb4</i>	GGATGGCAAGAAAGAGGTAGTG	GTAGGTTCCCAGAAGGTGAATG
The sequences of RT-PCR primer used in this study		

(Continued on next page)

Continued

REAGENT or RESOURCE	SOURCE	IDENTIFIER
Gene	Forward primer	Reverse primer
<i>Fn1</i>	ATGTGGACCCCTCCTGATAGT	GCCCCAGTGATTTCAGCAAAGG
Biological samples		
Mouse sample	This paper	N/A
Bacterial and virus strains		
DH5 α		TSV-A07
Chemicals, peptides, and recombinant proteins		
DMED/F12(1:1) basic(1X)	GIBCO	Cat# C11330500BT
DMEM	GIBCO	Cat# C11995500BT
Penicillin/Streptomycin	GIBCO	Cat# 15140-122
GlutaMAX	GIBCO	Cat# 35050-061
B27	GIBCO	Cat# A3582801
N ₂	GIBCO	Cat# 17502048
N-acetylcysteine	Sigma	Cat# A9165
Nicotinamide	Sigma	Cat# N0636
EGF	Peprotech	Cat# AF-100-15-1000
Noggin	Peprotech	Cat# 120-10C-250
FGF10	Peprotech	Cat# 100-26-1000
R-spondin-1	Peprotech	Cat# 120-38-1000
A83-01	Peprotech	Cat# 9094360
TrypLE™	GIBCO	Cat# 12604-028
T7E1	Vazyme	Cat# EN303-01
Protein kinase K	Solarbio	Cat# P9460
D-luciferin potassium salt	Biovision	Cat# 7903-10PK
Matrigel	Corning	Cat# 356237
TRIzol	Applied Biosystems	Cat# 15596026
Collagenase I	GIBCO	Cat# 17100-017
Collagenase IV	GIBCO	Cat# 17104-019
SYBR	Applied Biosystems	Cat# A25741
DMSO	MPbio	Cat# 196055
DPBS	GIBCO	Cat# C14190500BT
FBS	Multicell	Cat# 086-150
Trypsin	GIBCO	Cat# 25200-072
Protease inhibitors	Beyotime	Cat# P1045
Library preparation and sequencing reagents		
Chromium™ Single Cell 3' Library & Gel Bead Kit v3	10x Genomics	Cat# PN-1000075
Deposited data		
Data files for Omics data (raw data of RNA-seq and scRNA-seq) of this paper	GEO	GSE188761
Genetic alteration information of 8 stomach adenocarcinoma studies	cBioportal	https://www.cbioportal.org/
scRNA-seq of GC patients	(Sathe et al., 2020)	https://dna-discovery.stanford.edu/research/datasets/
TCGA STAD cohort	TCGA	https://portal.gdc.cancer.gov/
MDACC cohort	GEO	GSE28541
Normal mouse stomach tissues	GEO	GSE118083

(Continued on next page)

Continued

REAGENT or RESOURCE	SOURCE	IDENTIFIER
Experimental models: Cell lines		
Mouse: RAW264.7 Cells	ATCC	Cat# TIB-71, RRID: CVCL_0493
Human: HEK-293T	ATCC	Cat# CRL-1573, RRID: CVCL_0045
Oligonucleotides		
CRISPR sgRNAs see Table S5	DNA2.0	https://www.atum.bio/eCommerce/cas9/input
PCR and RT-qPCR primer, see Table S5	N/A	https://sg.idtdna.com/PrimerQuest/Home/Index
Recombinant DNA		
psPAX2	Addgene	RRID: Addgene_12260
pMD2.G	Addgene	RRID: Addgene_12259
V2TC-sgRNA	(Na et al., 2022)	N/A
PIL-Myc-Luci2	(Na et al., 2022)	N/A
pMSCV-dCas9-VP64-p65-Rta	(Hang et al., 2022)	N/A
Software and algorithms		
Code generated for this study	This paper	https://github.com/AilingZhong/GC_TME_Project
Cellranger (v.3.0.0)	10x Genomics	https://support.10xgenomics.com/single-cell-gene-expression/software
ClusterProfiler	(Yu et al., 2012)	https://guangchuangyu.github.io/software/clusterProfiler/
DESeq2	(Love et al., 2014)	https://bioconductor.org/packages/release/bioc/html/DESeq2.html
Pheatmap	bioconductor	https://cran.r-project.org/web/packages/pheatmap/
ggplot2	bioconductor	https://cran.r-project.org/package=ggplot2
Ggpubr	CRAN	https://rpkgs.datanovia.com/ggpubr/
GSEA	(Subramanian et al., 2005)	https://www.gsea-msigdb.org/gsea/index.jsp
Samtools	(Li et al., 2009)	https://github.com/samtools/samtools
Seurat (v3)	(Stuart et al., 2019)	https://satijalab.org/seurat/
SingleR	(Aran et al., 2019)	https://github.com/dviraran/SingleR
STAR	(Dobin et al., 2013)	https://github.com/alexdobin/STAR
URD	(Farrell et al., 2018)	https://github.com/farrellja/URD
iTALK	(Wang et al., 2019)	https://github.com/Coolgenome/iTALK
ImageJ	(Schneider et al., 2012)	https://imagej.nih.gov/ij/ ; RRID:SCR_003070
GSVA	(Hanzelmann et al., 2013)	https://github.com/rcastelo/GSVA
Survival	bioconductor	https://cran.r-project.org/web/packages/survival
Survminer	bioconductor	https://cran.r-project.org/web/packages/survminer
Snapgene	Snapgene	https://www.snapgene.com
Graphpad Prism 9	Graphpad Software	www.graphpad.com/scientific-software/prism/
FlowJo v10	FlowJo LLC	www.flowjo.com

RESOURCE AVAILABILITY

Lead contact

Further information and requests for resources and reagents should be directed to and will be fulfilled by the lead contact, Chong Chen (chongchen@scu.edu.cn).

Materials availability

All unique reagents generated in this study are available from the [lead contact](#) with a completed Materials Transfer Agreement.

Data and code availability

The bulk RNA-seq and scRNA-seq data in this study are deposited in NCBI GEO: GSE188761. The analysis codes can be found in GitHub (https://github.com/AilingZhong/GC_TME_Project). These accession numbers for the datasets are listed in the [key resources table](#). Any additional information required to reanalyze the data reported in this work paper is available from the [lead contact](#) upon request.

EXPERIMENTAL MODELS AND SUBJECTS DETAILS**Mice**

All the animal experiment protocols were approved by the Animal Care and Use Committee of Sichuan University. *Trp53*^{-/-} mice and Cas9-EGFP mice were purchased from Jackson Laboratories (Cat# 002,101 and 026179, RRID: IMSR_JAX:026179, respectively). Nude mice were purchased from Beijing HuaFukang Biological Technology Co. Ltd (6-8-week old, male). All of these mice were bred and kept in SPF animal facility of Sichuan university.

METHOD DETAILS**Organoid culture**

Normal mice stomach was harvested and washed with ice-cold DPBS (GIBCO, Cat# C14190500BT), then mechanically minced into pieces of 5-mm³ cubes and incubated in DPBS with 2.5 mM EDTA on ice. After incubation, the released gastric gland fractions were resuspended with Matrigel (Corning, Cat# 356237) and seeded in 48-wells plate. Normal stomach organoids were cultured in the gastric organoid culture medium (DMEM/F12 (GIBCO, Cat# C11330500BT) with 2 mM GlutaMAX (GIBCO, Cat# 35050-061), 1% Penicillin and Streptomycin (GIBCO, Cat# 15140-122), 1× B27 (GIBCO, Cat# A3582801), 1× N₂ (GIBCO, Cat# 17502048), 10 mM Y-27632, 200 ng/mL FGF10 (Peprotech, Cat# 100-26-1000), 500 nM A-8301 (Peprotech, Cat# 9094360), 50 ng/mL mouse recombinant EGF (Peprotech, Cat# AF-100-15-1000), 100 ng/mL mouse recombinant noggin (Peprotech, Cat# 120-10C-250), 10 mM Nicotinamide (Sigma, Cat# N0636), 1 mM N-acetylcysteine (Sigma, Cat# A9165), 10% Wnt3a condition medium, 10% R-spondin1 condition medium). Tumor tissues were harvested and washed with ice-cold DPBS, and then minced into pieces. Incubating the minced tumor tissue in digestion medium containing 0.5 mg/mL collagenase IV (GIBCO, Cat# 17104-019) and 1.0 mg/mL collagenase I (GIBCO, Cat# 17100-017) in DMEM/F12 medium at 37°C for 0.5 h. Tumor cells were collected by centrifugation and resuspended with Matrigel. Medium for tumor organoids was similar to gastric organoid culture medium but without Wnt3a. Organoid medium was refreshed every 2–3 days until passage.

Organoid genome editing

sgRNAs designed on the website of DNA2.0 Gene Design & Synthesis (<https://www.atum.bio/pipeline/dna>) were cloned into the lentiviral vector V2TC, which both expressed sgRNA and mCherry. These V2TC-sgRNA plasmids were transfected with the helper plasmids psPAX2 (RRID: Addgene_12260), pMD2.G (RRID: Addgene_12259) into HEK293T (ATCC, Cat# CRL-1573) cells by the calcium phosphate transfection method. 36 and 48 h's post-transfection, lentivirus containing supernatant was harvested and used for next experiments. Organoids were dissociated into single cells using TrypLE™ (GIBCO, Cat# 12604-028) and collected, then resuspended with lentivirus in 24-wells plate. The plate was centrifuged at 2000 rpm at 32°C for 1 h, then incubated for 2–3 h at 37°C. Polybrene (4 ng/mL) is added to enhance the efficiency of the lentiviral infection. After incubation, cells were resuspended with Matrigel and cultured as described above. Mutation validation was performed by the T7E1 (Vazyme, Cat# EN303-01) assay. All sgRNA sequences and primer sequences used in this study were listed in the [Table S6](#).

Organoid proliferation assay

Organoids were digested into single cells by TrypLE. 2,000 cells were seeded in a well of 96-wells plate. After 5 days culture, organoids were photographed (Olympus, IX73P2F). The size of organoids was measured using ImageJ (Version 1.51).

Antibodies

Antibodies of Recombinant Anti-Ki67 (Abcam Cat# ab16667, RRID: AB_302459), Anti-Cytokeratin 7 (Abcam Cat# ab181598, RRID: AB_2783822), Anti-ErbB2/HER2 (Abcam Cat# ab134182, RRID: AB_2893179), Anti-EPCAM (Abcam Cat# ab213500, RRID: AB_2884975), Anti-GFP (Abcam Cat# ab290, RRID: AB_303395), Anti-Fibronectin (Abcam Cat# ab6328, RRID: AB_30542), Anti-F4/80 (Abcam Cat# ab6640, RRID: AB_1140040), Anti-c-Myc (phospho S62) (Abcam Cat# ab185656) were from Abcam; CDK4 Polyclonal (Proteintech Cat# 11026-1-AP, RRID: AB_2078702) was from Proteintech; Cas9 (*S. pyogenes*) (E7M1H) XP® Rabbit mAb (Cell Signaling Technology Cat# 19526; RRID: AB_2798820), Sox2 (D9B8N) Rabbit mA (Cell Signaling Technology Cat# 23064, RRID: AB_2714146), PTEN (138G6) Rabbit (Cell Signaling Technology Cat# 9559, RRID: AB_390810) were from Cell Signaling Technology; Anti-beta Catenin (Thermo Fisher Scientific Cat# MA5-32540, RRID: AB_2809817) was from Thermo Fisher Scientific;

Anti-ITGB4 (Novus biologicals Cat# NBP2-38297) was from Novus biologicals; Anti-LGR5 Rabbit Polyclonal (OriGene Cat# TA324287) was from OriGene; CD45 (BioLegend Cat#109820, RRID: AB_492872), CD11b (BioLegend Cat#101216, RRID: AB_312799), F4/80 (BioLegend Cat#123132, RRID: AB_11203717) were purchased from BioLegend.

Western blotting

Organoid lysates were extracted in RIPA buffer (Beyotime, Cat# P0013) supplemented with protease inhibitors (Beyotime, Cat# P1045), followed by SDS-PAGE gel electrophoresis and blotting onto PVDF membranes (Millipore). Primary antibodies were applied at 1:1000-1:2000 dilution in 5% non-fatty milk and incubated overnight at 4°. HRP-conjugated secondary antibodies were applied at 1:10000 dilution. Images were obtained by NcmECL Ultra Reagent (NCM biotech).

Mouse model establishment

Both orthotopic and subcutaneous GC mouse model were generated in this study. Organoids were collected and aspirated into pre-chilled 29G insulin syringes. For the orthotopic model, 6 to 8-week-old male nude mice were anesthetized using isoflurane inhalation. The organoid suspension (2×10^5 cells per mouse) was directly injected into the submucosa of the lower third of the stomach. Mice was monitored weekly using bioluminescence imaging (PerkinElmer, IVIS spectrum). For the subcutaneous model, organoid suspension (2×10^5 cells per mouse) was injected into 6 to 8-week-old male nude mice subcutaneously. The size of the tumor was measured by calipers.

H&E, immunohistochemistry and immunofluorescence staining

Fresh tumor tissues were fixed in 4% paraformaldehyde, embedded in paraffin, and cut into 5 μ m sections (Leica RM2125 RTS Manual Microtome, RRID:SCR_018040). H&E staining was performed according to the standard protocol. For immunohistochemistry (IHC) and immunofluorescence (IF) staining, primary antibodies were applied as the protocol. A two-step detection kit (ZSGB-BIO, Cat# PV-9001 and Cat# PV-9002) was used for IHC, and hematoxylin for nuclear staining. Imaging was performed by Pannoramic MIDI. As for the IF staining, fluorescence-conjugated secondary antibodies were applied at 1:500-1:1000 dilution. Imaging was performed using fluorescence microscopy (Zeiss, 880).

CRISPRa system

The CRISPRa system used in this study was CRISPR-dCas9-VPR (Chavez et al., 2015), which has a retrovirus-based backbone as pMSCV-dCas9-VP64-p65-Rta (Hang et al., 2022). The system was used to upregulate *Fn1* in RAW 264.7 (ATCC, Cat# TIB-71). The sgRNA-BFP plasmid was derived from the lentiCRISPR v2 plasmid (RRID: Addgene_52961) by replacing the sequence of Cas9 with BFP. *Fn1* sgRNA candidates for CRISPRa were design using DNA2.0. The gene expression of *Fn1* was measured by qPCR.

RNA extraction and RT-qPCR

Total RNA extraction using TRIzol reagent (Applied Biosystems, Cat# 15596026) and complementary DNA (cDNA) synthesis using M-MLV Reverse Transcriptase (Invitrogen, Cat# 28025013) were performed under the manufacturer's instructions. Real-time quantitative PCR (RT-qPCR) was performed using PowerupTM SYBR Green Master Mix (Applied Biosystems, Cat# A25741) in QuantStudioTM 3 (Applied Biosystems), *Fn1* gene primers for RT-qPCR were listed in Table S6.

Wound-healing assay

Cell migration ability was determined using a wound-healing assay. Macrophage cell line RAW 264.7 and TMPC tumor cells were co-cultured at a 1:1 ratio. After cells reached 90% confluence, a pipette tip was used to scratch the cell monolayer across the center of each well. Detached cells were washed with DPBS, and serum-free medium was added. Images were taken at 0 h and 36 h following media replacement, wound areas were measured using ImageJ.

Tumor-macrophage co-culture assay

RAW 264.7 cells and TMPC tumor cells were co-cultured at a 1:1 ratio in RPMI 1640 medium (GIBCO, Cat# C11875500) with 10% FBS (WISENT, Cat# 086-150). After 4 h of co-culture, the cells adhesion between RAW 264.7 cells (blue) and tumor cells (red) were observed and photographed. ImageJ was used to count the total numbers of tumor cells and macrophages. And tumor-macrophage interactions were calculated as the percentages of adjacent tumor-macrophages in total numbers of tumor and macrophages.

Macrophages depletion *in vivo*

Orthotopic TMPC gastric cancer mice (6-8-weeks old) were randomly divided into two groups. Mice was treated with PBS-liposome solution and clodronate-liposome solution (LIPOSOMA, CP-010-010), respectively, by weekly tail vein injection. Tumor burden in mice was monitored using bioluminescence imaging.

Flow cytometry

Spleen was obtained from orthotopic TMPC gastric cancer mice. Then spleen was crushed and filtered with 100 μ m filter membrane to obtain single cells, and RBCs were lysed by ACK lysis buffer on ice. CD45 (BioLegend, Cat# 109,820, 1:200), CD11b (BioLegend, Cat# 101216, 1:200), and F4/80 (BioLegend, Cat# 123132, 1:200) staining were performed at 4°C for 30 min. Flow cytometry analysis was performed on Fortessa machines (BD Bioscience) and analyzed with Flowjo.

RNA-seq analyses

Two months after subcutaneous (TM, TMP, and TMPC) and orthotopic (TMPC) transplantation, the mice were sacrificed to obtain their tumor tissue, and about 1cm³ tissue was taken for database construction. RNA libraries were prepared using standard Illumina protocols. Transcriptome sequencing was performed by an Illumina NovaSeq 6000 sequencing platform with 150 bp paired-end sequencing. After adapters, ploy-N, and low-quality reads removal, clean data were aligned to the mouse reference genome (mm10) by STAR_2.6.0. Transcript abundances, significance levels and differentially expressed genes were generated and identified by DESeq2 (v.1.22.2) (RRID:SCR_015687). The significantly up-regulated genes in each group were used to perform Gene Ontology (RRID:SCR_002811) enrichment analyses with the R package clusterProfiler (v. 3.10.1) (RRID:SCR_016884). GSEA (RRID:SCR_003199) was utilized to identify the significantly enriched pathways by default parameters. Preranked function was performed to clarify the overall transcriptome similarity between mouse models and tumor tissues of GC patients. Pheatmap (v.1.0.12) (RRID:SCR_016418) was used to visualize differentially expressed genes with z scores.

scRNA-seq analyses

Orthotopic and subcutaneous tumor tissues were removed from recipient mice and cut up with sterile scissors. Then tissues were dissociated into 15 mL conical tubes by pipetting and resuspension in TrypLE™ (GIBCO, Cat#12604-028) for 1 h at 37°C, until all were single cells under the microscope and centrifuged at 600 g for 10 min. Cells were resuspended with 4% BSA solution on ice. Single cell RNA-seq libraries were constructed by Chromium Single Cell 3' Reagent kits v.3 following the manufacturer's protocol (10x Genomics). Illumina NovaSeq 6000 platform was utilized for transcriptome sequencing. To distinguish tumor cells from non-tumor cells, we added exogenous sequence of vectors (Cas9, V2TC, and LUCI2LTR) into mouse reference genome(mm10), and CellRangerV3 was performed for sequencing alignment and quantification. The Seurat (v.3.1.5) (RRID:SCR_016341) pipeline was implemented for downstream analyses. Cells with more than 25% mitochondrial counts or detected genes lower than 200 or above 7,500 were recognized as low quality cells or potential doublets, which were filtered out. Gene expression matrices of the remaining cells were integrated by Seurat function "merge". After data normalization, 'vst' mode of "FindVariableFeatures" function was performed for high virable genes detection. UMAP and URD were performed for cells dimensionality reductions. "FindMarkers" function of Seurat was implemented for differentially expressed genes ($p\text{-adj} < 0.05$ and absolute avg.logFC > 0.25) identification in each subpopulations. Gene Ontology (RRID:SCR_002811) enrichments were calculated and visualized by the R package clusterProfiler (RRID:SCR_016884). GSVA (RRID:SCR_021058) and limma (RRID:SCR_010943) were performed to calculate the pathway scores and significance levels (FDR < 0.01). Expression patterns were visualized with the R package pheatmap (RRID:SCR_016418). LandSCENT was used to calculate and quantify the entropy signaling in each cell based on the net13Jun12.m protein-protein network.

Cell-cell interaction analyses

To illustrate the global differences of microenvironment between subcutaneous and orthotopic tumors, iTALK was employed to identify the most possible factors which could mediate tumor metastasis. For candidate ligand genes, differentially expressed genes ($p\text{-adj} < 0.05$ and absolute log₂FoldChange > 0.25) were identified between subcutaneous and orthotopic samples for each non-tumor subpopulation by FindMarkers function of Seurat, then we matched them from the iTALK database to find the differentially expressed ligand genes. As for receptor genes, since we focused on the effect of non-tumor cells on tumor cells, the genes with the highest expression weight ($p\text{-adj} < 0.05$ and absolute log₂FoldChange > 0.25) in the tumor cell population were selected as the potential tumor receptor genes comparing to non-tumor cells. Candidate ligands (n = 200) and receptors (n = 26) were then constructed a putative cell-cell communication network by iTALK. An interaction score which was defined as the product of the expression difference between orthotopic and subcutaneous non-tumor cell population and log₂ fold-change of tumor receptors (comparing tumor cells to other non-tumor cell populations) was used to rank these interactions. Finally, we acquired the top candidate ligand-receptor pairs and compared their expression levels between subcutaneous and orthotopic cell clusters. p values were determined by Wilcoxon rank-sum test.

Clinical correlation analyses

TCGAAbiolinks (RRID:SCR_017683) was used to download the transcriptome data and clinical information of the TCGA-STAD cohort. Patients without paired omics and clinical data were filtered in this study. The MDACC transcriptome matrix and corresponding clinical prognostic information were downloaded from GSE2851 (Oh et al., 2018). The scRNA-seq data of human GC were downloaded from <https://dna-discovery.stanford.edu>. To demonstrate the consistency and difference of transcriptome programming between GC patients and mouse models. Firstly, GC patients' transcriptome data of the TCGA-STAD cohort were divided into adjacent-normal or tumor samples according to the clinical information. And the TM mouse was diagnosed as premalignant and the TMP and TMPC as malignant type. Then we used DESeq2 (RRID:SCR_015687) standard pipeline to get the differentially expressed genes

($p < 0.05$) by comparing human normal with tumor samples, mouse TM with TMP&TMPC group, separately. The R package gmp was used to calculate the significant level of overlaps based on the hypergeometric test. And enrichment scores were calculated from the proportion of overlapped gene counts. And singleR was used to calculate the similarity between mouse and human GC in the single-cell resolution. The fine-tuning data were used to quantify the correlation coefficient in each cell type on the whole transcriptome between mouse and human gastric cancer. To better understand the metastasis mechanism in the TCGA-STAD cohort, patients with clear metastasis stages information (M0 or M1) were divided into different subgroups based on the distribution of gene signatures, and those with unknown metastasis stages were filtered. Then, significantly up-regulated genes in patients with metastasis (M1) were defined as metastasis signature genes comparing to those without metastasis (M0). Alluvial maps were used to visualize the results of patient molecular classification.

Survival analyses

The R package survival and survminer were used to divide patients into subgroups based on the expression levels of specific-gene or gene signature scores. Besides, the Kaplan–Meier plots were quantified and visualized by survminer, log rank test to calculate p values between groups.

QUANTIFICATION AND STATISTICAL ANALYSIS

Zeiss software was used to analyze the nuclear and cytoplasmic distribution of proteins. Densitometric scanning of ImageJ software (version 1.51) was used to quantify immunoblots. GraphPad (version 9.0.0) or R package ggpubr were used for the statistical analysis, detailed statistical tests used were named within the text. p -value < 0.05 was considered statistically significant.